

A 38 Million Year Old Mini-Neptune in the Kepler Field

L. G. BOUMA ^{1, 2, *} J. L. CURTIS ^{3, 4} K. MASUDA ⁵ L. A. HILLENBRAND, ² G. STEFANSSON ^{6, 1, †}
H. ISAACSON ⁶ N. NARITA ^{7, 8, 9, 10} A. FUKUI ^{7, 10} M. IKOMA ¹¹ M. TAMURA ^{12, 9, 13}
A. L. KRAUS ¹⁴ E. FURLAN ¹⁵ C. L. GNILKA ^{16, 15} K. V. LESTER ¹⁶ AND S. B. HOWELL ¹⁶

¹Department of Astrophysical Sciences, Princeton University, 4 Ivy Lane, Princeton, NJ 08540, USA

²Cahill Center for Astrophysics, California Institute of Technology, Pasadena, CA 91125, USA

³Department of Astronomy, Columbia University, 550 West 120th Street, New York, NY 10027, USA

⁴Department of Astrophysics, American Museum of Natural History, New York, NY 10024, USA

⁵Department of Earth and Space Science, Osaka University, Osaka 560-0043, Japan

⁶Astronomy Department, University of California, Berkeley, CA 94720, USA

⁷Komaba Institute for Science, The University of Tokyo, Tokyo 153-8902, Japan

⁸Japan Science and Technology Agency, PRESTO, Tokyo 153-8902, Japan

⁹Astrobiology Center, Tokyo 181-8588, Japan

¹⁰Instituto de Astrofísica de Canarias (IAC), 38205 La Laguna, Tenerife, Spain

¹¹Division of Science, National Astronomical Observatory of Japan, Tokyo 181-8588, Japan

¹²Department of Astronomy, University of Tokyo, Tokyo 113-0033, Japan

¹³National Astronomical Observatory of Japan, Tokyo 181-8588, Japan

¹⁴Department of Astronomy, The University of Texas at Austin, Austin, TX 78712, USA

¹⁵NASA Exoplanet Science Institute, Caltech/IPAC, Pasadena, CA 91125, USA

¹⁶NASA Ames Research Center, Moffett Field, CA 94035, USA

(Received 2021 Oct 12; Revised —; Accepted —)

Submitted to AAS Journals

ABSTRACT

Kepler 1627A is a G8V star previously known to host a $3.8 R_{\oplus}$ mini-Neptune on a 7.2 day orbit. The star was observed by the Kepler space telescope because it is nearby ($d = 329$ pc) and it resembles the Sun. Here we show using Gaia kinematics, TESS stellar rotation periods, and spectroscopic lithium abundances that Kepler 1627 is a member of the 38^{+6}_{-5} Myr old δ Lyr cluster. To our knowledge, this makes Kepler 1627Ab the youngest planet with a precise age yet found by the main Kepler mission. The Kepler photometry shows two peculiarities: the average transit profile is asymmetric, and the individual transit times might be correlated with the local light curve slope. We discuss possible explanations for each anomaly. More importantly, the δ Lyr cluster is one of $\sim 10^3$ coeval groups whose properties have been clarified by Gaia. Many other exoplanet hosts are candidate members of these clusters; these memberships can be verified with the trifecta of Gaia, TESS, and ground-based spectroscopy.

Keywords: exoplanet evolution (491), open star clusters (1160), stellar ages (1581)

1. INTRODUCTION

While thousands of exoplanets have been discovered orbiting nearby stars, the vast majority of

them are several billion years old. This makes it difficult to test origin theories for the different families of planets, since many evolutionary processes are expected to operate on timescales of less than 100 million years.

For instance, the “mini-Neptunes”, thought to be made of metal cores, silicate mantles (Kite et al. 2020), and extended hydrogen-dominated atmospheres, are expected to shrink in size by fac-

Corresponding author: L. G. Bouma
luke@astro.caltech.edu

* 51 Pegasi b Fellow

† Henry Norris Russell Fellow

tors of several over their first 10^8 years. Specifically, in the models of Owen & Wu (2016) and Owen (2020), the $\approx 5 M_\oplus$ planets start with sizes of $4 - 12 R_\oplus$ shortly after the time of disk dispersal ($\lesssim 10^7$ years), and shrink to sizes of $2 - 4 R_\oplus$ by 10^8 years. While the majority of this change is expected to occur within the first few million years after the disk disperses (Ikoma & Hori 2012), stellar irradiation and internal heat can also power gradual outflows which, if strong enough, can deplete or entirely strip the atmosphere (Owen & Wu 2013; Ginzburg et al. 2018). Discovering young planets, measuring their masses, and detecting their atmospheric outflows are key steps toward testing this paradigm, which is often invoked to explain the observed radius distribution of mature exoplanets (Fulton et al. 2017; Van Eylen et al. 2018).

The K2 and TESS missions have now enabled the detection of about ten close-in planets younger than 100 million years, all smaller than Jupiter (Mann et al. 2016; David et al. 2016, 2019; Newton et al. 2019; Bouma et al. 2020; Plavchan et al. 2020; Rizzuto et al. 2020; Martioli et al. 2021). The Kepler mission however has not yielded any planets with precise ages below one gigayear (Meibom et al. 2013). The reason is that during the main Kepler mission (2009–2013), only four open clusters were known in the Kepler field, with ages spanning 0.7 Gyr to 9 Gyr (Meibom et al. 2011). Though isochronal, gyrochronal, and lithium-based analyses suggest that younger Kepler planets do exist (Berger et al. 2018; David et al. 2021), accurate and precise age measurements typically require an ensemble of stars. Fortunately, recent analyses of the Gaia data have greatly expanded our knowledge of cluster memberships (e.g., Cantat-Gaudin et al. 2018; Zari et al. 2018; Kounkel & Covey 2019; Meingast et al. 2021; Kerr et al. 2021). As part of our Cluster Difference Imaging Photometric Survey (CDIPS, Bouma et al. 2019), we concatenated the available analyses from the literature, which yielded a list of candidate young and age-dated stars (see Appendix A).

Matching our young star list against stars observed by Kepler revealed that Kepler observed a portion of the δ Lyr cluster (Stephenson-1; Theia 73). More specifically, a clustering analysis of the Gaia data by Kounkel & Covey (2019) reported that Kepler 1627 (KIC 6184894; KOI 5245) is a δ Lyr cluster member. Given the previous statistical validation of the close-in mini-Neptune Kepler 1627b (Tenenbaum et al. 2012; Morton et al. 2016; Thompson et al. 2018), we begin by scrutinizing the properties of the cluster (Section 2). We find that the δ Lyr cluster is 38^{+6}_{-5} Myr old, and in Section 3 show that Kepler 1627 is both a binary

and also a member of the cluster. Focusing on the planet (Section 4), we confirm that despite the existence of the previously unreported M2.5V companion, hereafter Kepler 1627B, the planet orbits the G-dwarf primary, Kepler 1627A. We also analyze an asymmetry in the average transit profile, and a possible correlation between the individual transit times and the local light curve slope. We conclude by discussing broader implications for our ability to age-date a larger sample of planets (Section 5).

2. THE CLUSTER

To measure the age of the δ Lyr cluster, we first selected a set of candidate cluster members (Section 2.1), and then analyzed these stars using a combination of the isochronal and gyrochronal techniques (Section 2.2).

2.1. Selecting Cluster Members

Kounkel & Covey (2019) applied an unsupervised clustering algorithm to Gaia DR2 on-sky positions, proper motions, and parallaxes for stars within the nearest kiloparsec. For the δ Lyr cluster (Theia 73), they reported 3,071 candidate members. We matched these stars against the latest Gaia EDR3 observations using the dr2_neighbourhood table from the ESA archive, taking the stars closest in proper motion and epoch-corrected angular distance as the presumed match (Gaia Collaboration et al. 2021a). In Figure 1, have shown galactic positions only for the stars with parallax signal-to-noise exceeding 20. The reported cluster members (gray and black points) extend over a much larger volume than the cluster previously identified by Stephenson (1959) and later corroborated by Eggen (1968). While the non-uniform “clumps” of stars might comprise a *bona fide* cluster of identically-aged stars, they could also be heavily contaminated by field stars. We therefore considered stars only in the immediate kinematic and spatial vicinity of Kepler 1627 as candidate cluster members. We performed the selection cuts manually, by drawing lassos with the interactive glue visualization tool (Beaumont et al. 2014) in the four projections shown in Figure 1. The overlap between the Kepler field and the resulting candidate cluster members is shown in Figure 2. While this method will include some field interlopers in the “cluster star” sample, and vice-versa, it should suffice for our aim of verifying the existence of the cluster in the vicinity of Kepler 1627.

2.2. The Cluster’s Age

2.2.1. Color-Absolute Magnitude Diagram

We measured the isochrone age using an empirical approach. The left panel of Figure 3 shows

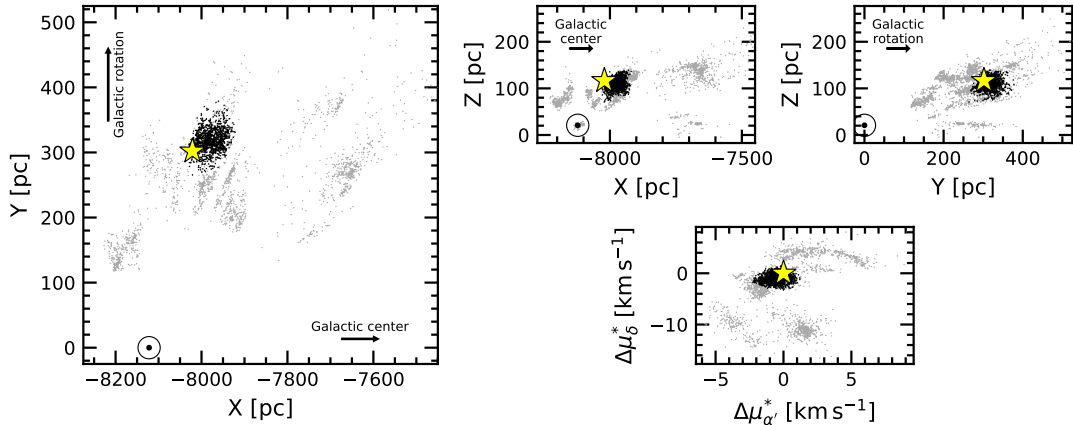


Figure 1. Galactic positions and tangential velocities of stars in the δ Lyr cluster. Points are reported cluster members from Kounkel & Covey (2019). The tangential velocities relative to Kepler 1627 (bottom right) are computed assuming that every star has the same three-dimensional spatial velocity as Kepler 1627. Our analysis considers stars (black points) in the spatial and kinematic vicinity of Kepler 1627 (yellow star). The question of whether the other candidate cluster members (gray points) are part of the cluster is outside our scope. The location of the Sun (\odot) is shown.

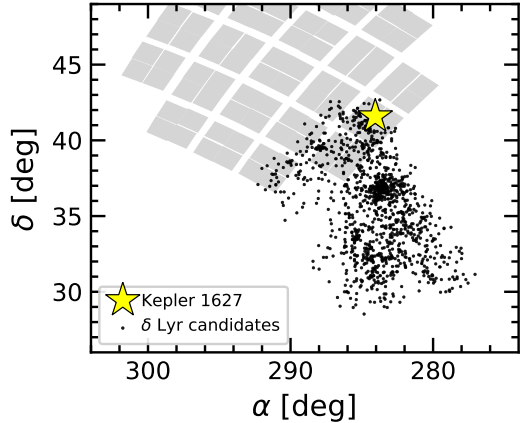


Figure 2. Kepler's view of the δ Lyr cluster, shown in equatorial coordinates. Each black circle is a candidate cluster member selected based on its position and kinematics (Figure 1). Of the 1,201 candidate cluster members, 58 have at least one quarter of Kepler data. TESS has also observed most of the cluster, for one to two lunar months to date.

the color-absolute magnitude diagram (CAMD) of candidate δ Lyr cluster members, IC 2602, the Pleiades, and the field. The stars from the Pleiades and IC 2602 were adopted from Cantat-Gaudin et al. (2018), and the field stars are from the Gaia EDR3 Catalog of Nearby Stars (Gaia Collaboration et al. 2021b). We cleaned these following the data filtering criteria from Gaia Collaboration et al. (2018a, Appendix B), except that we weakened the parallax precision requirement to $\varpi/\sigma_\varpi > 5$. These filters were designed to include genuine binaries while omitting instrumental artifacts. We then corrected for extinction by querying the 3-dimensional maps of Capitaino et al. (2017) and Lallement

et al. (2018)¹, and applied the extinction coefficients $k_X \equiv A_X/A_0$ computed by Gaia Collaboration et al. (2018a) assuming that $A_0 = 3.1E(B-V)$. For IC 2602, the Pleiades, and the δ Lyr cluster, this procedure yielded a respective mean and standard deviation for the reddening of $E(B-V) = \{0.020 \pm 0.003, 0.045 \pm 0.008, 0.032 \pm 0.006\}$. These values agree reasonably well with previously reported values from the literature (e.g., Gaia Collaboration et al. 2018a; Kounkel & Covey 2019; Bossini et al. 2019).

Figure 3 shows that the δ Lyr cluster and IC 2602 overlap, and therefore are approximately the same age. In our exploration, we also compared against μ -Tau (62 ± 7 Myr; Gagné et al. 2020) and the Upper-Centaurus-Lupus (UCL) component of the Sco OB2 association (≈ 16 Myr; Pecaut & Mamajek 2016). The pre-main-sequence M dwarfs of the δ Lyr cluster were intermediate between the latter two clusters. To turn this heuristic interpolation into an age measurement, we used the empirical method developed by Gagné et al. (2020). In brief, we fitted the pre-main-sequence loci of a set of reference clusters, and the locus of the target δ Lyr cluster was then modeled as a piecewise linear combination of these reference clusters. For our reference clusters, we adopted members of UCL, IC 2602, and the Pleiades from Damiani et al. (2019) and Cantat-Gaudin et al. (2018) respectively. We removed binaries by requiring $\text{RUWE} < 1.3$, $\text{radial_velocity_error}$ below the 80th percentile of each cluster's distribution, and excluded stars that were obvious photometric binaries in the CAMD. We then passed a

¹ <https://stilism.obspm.fr/>, 2021/09/25

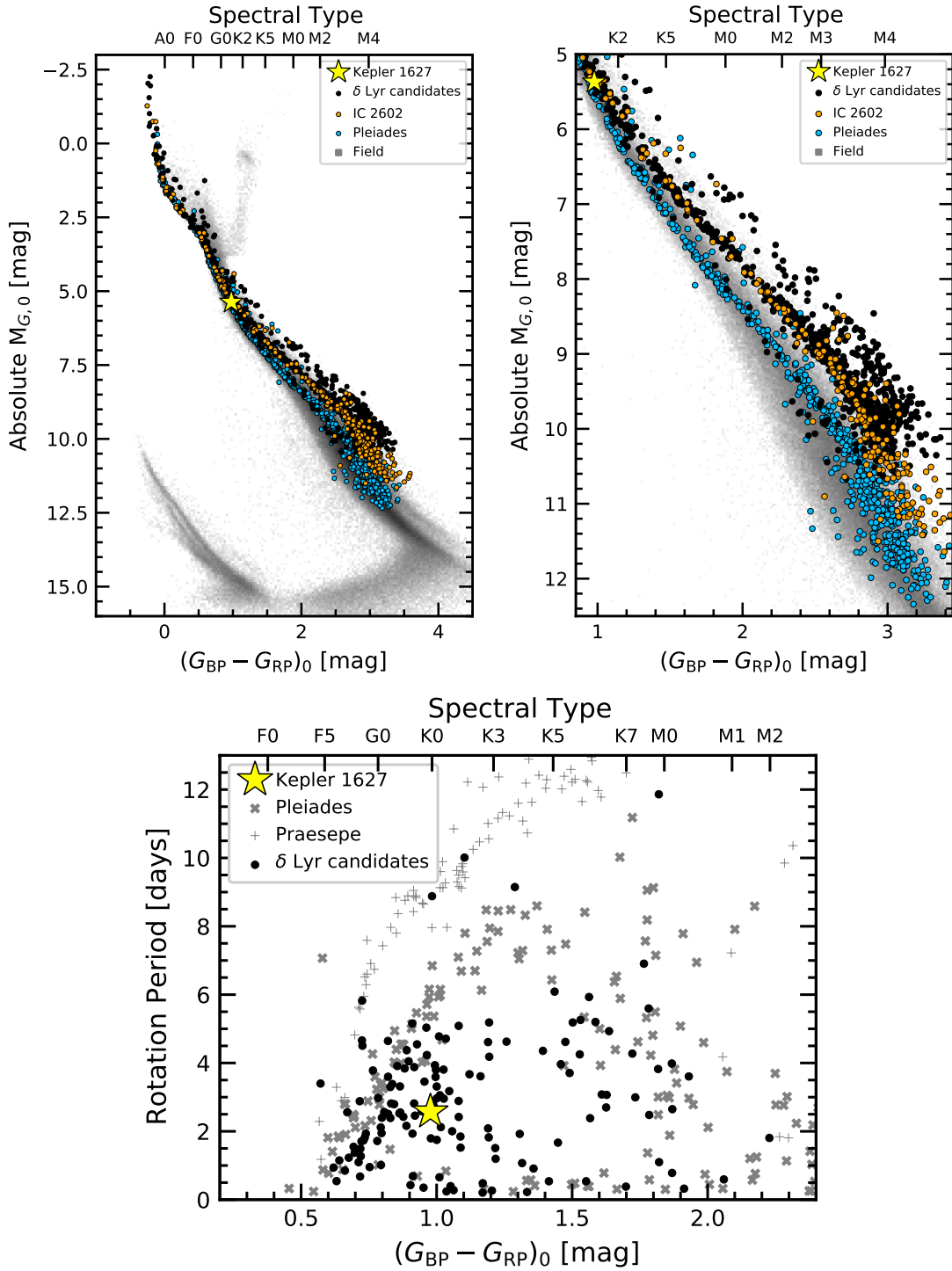


Figure 3. The δ Lyr cluster is 38^{+6}_{-5} Myr old. *Top:* Color-absolute magnitude diagram of candidate δ Lyr cluster members, in addition to stars in IC 2602 (≈ 38 Myr), the Pleiades (≈ 115 Myr), and the Gaia EDR3 Catalog of Nearby Stars (gray background). The zoomed right panel highlights the pre-main-sequence. The δ Lyr cluster and IC 2602 are approximately the same isochronal age. *Bottom:* TESS and Kepler stellar rotation period versus dereddened Gaia color, with the Pleiades and Praesepe (650 Myr) shown for reference (Rebull et al. 2016; Douglas et al. 2017). Most candidate δ Lyr cluster members are gyrochronologically younger than the Pleiades; outliers are probably field interlopers.

206 moving box average and standard deviation across
 207 the CAMD in 0.10 mag bins, fitted a univariate
 208 spline to the binned values, and assembled a piece-
 209 wise grid of hybrid isochrones spanning the ages
 210 between UCL to the Pleiades using Equations 6
 211 and 7 from Gagné et al. (2020).

212 The ages returned by this procedure depend on
 213 the ages assumed for each reference cluster. We
 214 adopted a 115 Myr age for the Pleiades (Dahm
 215 2015), and a 16 Myr age for UCL (Pecaut &
 216 Majajek 2016). The age of IC 2602 however is the
 217 most important ingredient, since it receives the
 218 most weight in the interpolation. Plausible ages
 219 for IC 2602 span 30 Myr to 46 Myr, with older ages
 220 being preferred by the lithium-depletion-boundary
 221 (LDB) measurements (Dobbie et al. 2010; Randich
 222 et al. 2018) and younger ages by the main-
 223 sequence turn-off (Stauffer et al. 1997; David &
 224 Hillenbrand 2015; Bossini et al. 2019). If we were
 225 to adopt the 30 Myr age for IC 2602, then the δ
 226 Lyr cluster would be 31^{+5}_{-4} Myr old. For the con-
 227 verse extreme of 46 Myr, the δ Lyr cluster would
 228 be 44^{+8}_{-7} Myr old. We adopt an intermediate 38 Myr
 229 age for IC 2602, which yields an age for the δ Lyr
 230 cluster of 38^{+6}_{-5} Myr.² Follow-up studies of the LDB
 231 or main-sequence turn-off in the δ Lyr cluster could
 232 help determine a more precise and accurate age for
 233 the cluster, and are left for future work.

2.2.2. Stellar Rotation Periods

234 Of the 3,071 candidate δ Lyr cluster members
 235 reported by Kounkel & Covey (2019), 924 stars
 236 were amenable to rotation period measurements
 237 ($G < 17$ and $(G_{\text{BP}} - G_{\text{RP}})_0 > 0.5$) using the TESS
 238 full frame image data. We extracted light curves
 239 from the TESS images using the nearest pixel to
 240 each star, and regressed them against systematics
 241 with the causal pixel model implemented in the
 242 unpopular package (Hattori et al. 2021). We
 243 then measured candidate rotation periods using a
 244 Lomb-Scargle periodogram (Lomb 1976; Scargle
 245 1982; Astropy Collaboration et al. 2018). To en-
 246 able cuts on crowding, we queried the Gaia source
 247 catalog for stars within a $21.^{\circ}0$ radius of the tar-
 248 get star (a radius of 1 TESS pixel). Within this ra-
 249 dius, we recorded the number of stars with greater
 250 brightness than the target star, and with brightness
 251 within 1.25 TESS magnitudes of the target star.

252 We then cleaned the candidate TESS rotation pe-
 253 riod measurements through a combination of au-
 254 tomated and manual steps. As a matter of scope, we

255 restricted our attention to the 391 stars discussed
 256 in Section 2.1 in the spatial and kinematic proxim-
 257 ity of Kepler 1627. Kepler rotation periods were
 258 derived by McQuillan et al. (2014) for 28 of these
 259 stars; for these cases, we simply adopted the Kepler
 260 rotation period. For the remaining stars with only
 261 TESS data, we focused only on the stars for which
 262 no companions were known with a brightness ex-
 263 ceeding one-tenth of the target star in a $21.^{\circ}0$ ra-
 264 dius. There were 192 stars that met these crowding
 265 requirements, and that had TESS data available.
 266 For plotting purposes we then imposed a selection
 267 based on the strength of the signal itself: we re-
 268 quired the Lomb Scargle power to exceed 0.2, and
 269 the period to be below 15 days.

270 The lower panel of Figure 3 shows the result-
 271 ing 145 stars. The majority of these stars fall be-
 272 low the “slow sequence” of the Pleiades, consist-
 273 ent with a gyrochronal age for the δ Lyr cluster
 274 below 100 Myr. In fact, the rotation-color distri-
 275 butions of other 30 Myr to 50 Myr clusters (e.g.,
 276 IC 2602 and IC 2391) are indistinguishable (Dou-
 277 glas et al. 2021). Approximately 10 of the δ Lyr
 278 cluster stars appear as outliers above the “slow se-
 279 quence”. Assuming that they are all false positives
 280 (i.e., field interlopers), our rotation period detec-
 281 tion fraction would be $135/192 \approx 70\%$. The other
 282 stars are likely to be field contaminants. A final
 283 possible confounding factor – binarity – is known
 284 to affect the “fast sequence” of stars beneath the
 285 slow sequence (Meibom et al. 2007; Gillen et al.
 286 2020; Bouma et al. 2021). We do not expect it to
 287 change the central conclusion regarding the clus-
 288 ter’s age.

3. THE STARS

3.1. Kepler 1627A

3.1.1. Age

290 Based on the spatial and kinematic association of
 291 Kepler 1627 with the δ Lyr cluster, and the assump-
 292 tion that the planet formed shortly after the star, it
 293 seems likely that Kepler 1627 is the same age as
 294 the cluster. There are two consistency checks on
 295 whether this is true: rotation and lithium. Based
 296 on the Kepler light curve, the rotation period is
 297 2.642 ± 0.042 days, where the quoted uncertainty
 298 is based on the scatter in rotation periods measured
 299 from each individual Kepler quarter. This is consis-
 300 tent with comparable cluster members (Figure 3).

301 To infer the amount of Li I from the 6708 \AA dou-
 302 blet (e.g., Soderblom et al. 2014), we acquired
 303 an iodine-free spectrum from Keck/HIRES on the
 304 night of 2021 March 26 using the standard setup
 305 and reduction techniques of the California Planet
 306 Survey (Howard et al. 2010). Following the equiv-
 307 alent width measurement procedure described by
 308 Bouma et al. (2021), we find $\text{EW}_{\text{Li}} = 233^{+5}_{-7} \text{ m}\text{\AA}$.

² Our exploration of the PARSEC and MIST isochrone models over a grid of ages, metallicities, and reddening, yielded the best agreement for this ≈ 38 Myr age as well, given $[\text{Fe}/\text{H}] = +0.1$ and $A_V = 0.2$ (Bressan et al. 2012; Choi et al. 2016); this preferred CAMD reddening is higher than the Lallement et al. (2018) value by a factor of two.

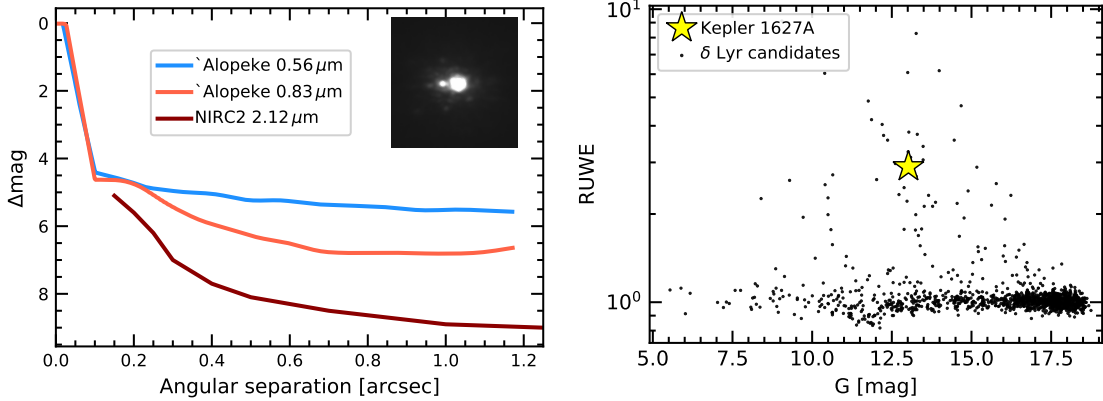


Figure 4. Kepler 1627 is a binary. *Left:* High-resolution imaging from Gemini-North/‘Alopeke and Keck/NIRC2 shows an \approx M2.5V companion at $\rho \approx 0.^{\prime\prime}16$, which corresponds to a projected separation of 53 ± 4 AU. The inset shows a cutout of the stacked NIRC2 image (North is up, East is left, scale is set by the separation of the binary). The lines show $5-\sigma$ contrast limits for the ‘Alopeke filters, and $6-\sigma$ contrast limits for NIRC2 outside of $0.^{\prime\prime}15$. *Right:* Gaia EDR3 renormalized unit weight error (RUWE) point estimates for candidate δ Lyr cluster members. Since other members of the cluster with similar brightnesses have comparable degrees of photometric variability, the high RUWE independently suggests that Kepler 1627 is a binary.

This value does not correct for the Fe I blend at 6707.44\AA . Nonetheless, given the stellar effective temperature (Table 1), this measurement is in agreement with expectations for a ≈ 40 Myr star (e.g., as measured in IC 2602 by Randich et al. 2018). It is also larger than any lithium equivalent widths measured by Berger et al. (2018) in their analysis of 1,301 Kepler-star spectra.

3.1.2. Stellar Properties

The adopted stellar parameters are listed in Table 1. The stellar mass, radius, and effective temperature are found by interpolating against a 38 Myr MIST isochrone (Choi et al. 2016). The statistical uncertainties are propagated from the absolute magnitude (mostly originating from the parallax uncertainty) and the color; the systematic uncertainties are taken to be the difference between the PARSEC (Bressan et al. 2012) and MIST isochrones. Reported uncertainties are a quadrature sum of the statistical and systematic components. As a consistency check, we analyzed the aforementioned Keck/HIRES spectrum from the night of 2021 March 26 using a combination of SpecMatch-Emp for stellar properties, and SpecMatch-Synth for $v\sin i$ (Yee et al. 2017). This procedure yielded $T_{\text{eff}} = 5498 \pm 100$ K, $\log g = 4.6 \pm 0.1$, $[\text{Fe}/\text{H}] = 0.15 \pm 0.10$ from SpecMatch-Emp, and $v\sin i = 18.9 \pm 1.0$ from SpecMatch-Synth. These values are within the $1-\sigma$ uncertainties of our adopted values from the isochrone interpolation.

3.2. Kepler 1627B

We first noted the presence of a close neighbor in the Kepler 1627 system on 2015 July 22 when we acquired adaptive optics imaging using the NIRC2 imager on Keck-II. We used the narrow camera ($\text{FOV} = 10.2''$) to obtain 8 images in the K' filter ($\lambda = 2.12\mu\text{m}$) with a total exposure time of 160 s. We analyzed these data following Kraus et al. (2016), which entailed using PSF-fitting to measure the separation, position angle, and contrast of the candidate companion. The best-fitting empirical PSF template was identified from among the near-contemporaneous observations of single stars in the same filter. The mean values inferred from the 8 images are reported in Table 1. To estimate the detection limits, we analyzed the residuals after subtracting the empirical PSF template. Within each residual image, the flux was measured through 40 mas apertures centered on every pixel, and then the noise as a function of radius was estimated from the RMS within concentric rings. Finally, the detection limits were estimated from the Strehl-weighted sum of the detection significances in the image stack, and we adopted the $6-\sigma$ threshold as the detection limit for ruling out additional companions.

We also observed Kepler 1627 on Gemini-North using the ‘Alopeke speckle imager on 2021 June 24. ‘Alopeke is a dual-channel speckle interferometer that uses narrow-band filters centered at $0.83\mu\text{m}$ and $0.56\mu\text{m}$. We acquired three sets of 1000×60 msec exposures during good seeing ($0.45''$), and used the autocorrelation function of these images to reconstruct a single image and $5-\sigma$ detection limits (see Howell et al. 2011). This procedure yielded a detection of the companion in

379 the $0.83\text{ }\mu\text{m}$ notch filter, but not the $0.56\text{ }\mu\text{m}$ filter.
 380 The measured projected separation and magnitude
 381 difference are given in Table 1.

382 Figure 4 summarizes the results of the high-
 383 resolution imaging. The Gaia EDR3 parallax for
 384 the primary implies a projected separation of $53 \pm$
 385 4 AU , assuming the companion is bound. Although
 386 the companion is unresolved in the Gaia source cat-
 387 alog (there are no comoving, codistant candidate
 388 companions brighter than $G < 20.5$ mag within
 389 $\rho < 120''$), its existence was also suggested by the
 390 primary star's large renormalized unit weight error
 391 (RUWE), relative to other members of the δ Lyr
 392 cluster. Based on the apparent separation, the bi-
 393 nary orbital period is of order hundreds of years.
 394 The large RUWE is therefore more likely to be
 395 caused by a PSF-mismatch skewing the Gaia cen-
 396 troiding during successive scans, rather than true
 397 astrometric motion. Regardless, given the low ge-
 398 ometric probability that a companion imaged at
 399 $\rho \approx 0''.16$ is a chance line-of-sight companion, we
 400 proceed under the assumption that the companion
 401 is bound, and that Kepler 1627 is a binary. Given
 402 the distance and age, the models of Baraffe et al.
 403 (2015) imply a companion mass of $M_B \approx 0.33M_\odot$
 404 and companion temperature of $T_{\text{eff},B} \approx 3450$ K.
 405 The corresponding spectral type is roughly M2.5V
 406 (Pecaut & Mamajek 2013). These models com-
 407 bined with the NIRC2 contrast limits imply physi-
 408 cal limits on tertiary companions of $M_{\text{ter}} < 50M_{\text{Jup}}$
 409 at $\rho = 50\text{ AU}$, $M_{\text{ter}} < 20M_{\text{Jup}}$ at $\rho = 100\text{ AU}$, and
 410 $M_{\text{ter}} < 10M_{\text{Jup}}$ at $\rho = 330\text{ AU}$.

4. THE PLANET

4.1. Kepler Light Curve

411 The Kepler space telescope observed Kepler 1627
 412 at a 30-minute cadence from 2009 May 2 until
 413 2013 April 8. Data gaps during quarters 4, 9, and
 414 13 led to an average duty cycle over the 3.9 year
 415 interval of 67%. Kepler 1627 was also observed at
 416 1-minute cadence from 2012 Oct 5 until 2013 Jan
 417 11. The top panel of Figure 5 shows a portion of the
 418 30-minute cadence PDCSAP light curve. Nonas-
 419 trophysical variability has been removed using the
 420 methods discussed by Smith et al. (2017); the
 421 default optimal aperture was assumed (Smith et al.
 422 2016). Cadences with non-zero quality flags (9%
 423 of the data) have been omitted. The resulting pho-
 424 tometry is dominated by a quasi-periodic starspot
 425 signal with a peak-to-peak amplitude that varies
 426 between 2% and 8%. Previous analyses have iden-
 427 tified and characterized the smaller transit signal
 428 (Tenenbaum et al. 2012; Thompson et al. 2018),
 429 validated its planetary nature (Morton et al. 2016),
 430 and even searched the system for transit timing
 431 variations (Holczer et al. 2016). Nonetheless, since
 432 the cluster membership provides us with more pre-

433 cise stellar parameters than those previously avail-
 434 able, we opted to reanalyze the light curve.

4.1.1. Transit and Stellar Variability Model

435 We fitted the Kepler long cadence time se-
 436 ries with a model that simultaneously included
 437 the planetary transit and the stellar variabil-
 438 ity. The stellar variability was modeled with
 439 the RotationTerm Gaussian Process kernel in
 440 exoplanet (Foreman-Mackey et al. 2020). This
 441 kernel assumes that the variability is generated by
 442 a mixture of two damped simple harmonic oscil-
 443 lators with characteristic frequencies set by $1/P_{\text{rot}}$
 444 and its first harmonic. We additionally included a
 445 jitter term to inflate the flux uncertainties in a man-
 446 ner that accounted for otherwise unmodeled excess
 447 white noise, and let the eccentricity float. For the
 448 limb-darkening, we assumed a quadratic law, and
 449 sampled using the uninformative prior suggested
 450 by Kipping (2013).

451 Our model therefore included 10 free parameters
 452 for the transit ($\{P, t_0, \delta, b, u_1, u_2, R_\star, \log g, e, \omega\}$), 2
 453 free parameters for the light curve normalization
 454 and a white noise jitter ($\{\langle f \rangle, \sigma_f\}$), and 5 hyper-
 455 parameters for the GP ($\{\sigma_{\text{rot}}, P_{\text{rot}}, Q_0, dQ, f\}$). We
 456 also considered including an additive SHOTerm
 457 kernel to account for stochastic noise, but found
 458 that this did not affect the results, and so opted for
 459 the simpler GP kernel. We fitted the models us-
 460 ing PyMC3 (Salvatier et al. 2016; Theano Devel-
 461 opment Team 2016), and accounted for the finite
 462 integration time of each exposure in the numerical
 463 integration when evaluating the model light curve
 464 (see Kipping 2010). We assumed a Gaussian like-
 465 lihood, and after initializing each model with the
 466 parameters of the maximum *a posteriori* model,
 467 we sampled using PyMC3's gradient-based No-U-
 468 Turn Sampler (Hoffman & Gelman 2014) in the
 469 bases indicated in Table 2. We used \hat{R} as our con-
 470 vergence diagnostic (Gelman & Rubin 1992).

471 Figure 5 shows the resulting best-fit model in or-
 472 ange (top) and purple (bottom). The model pa-
 473 rameters and their uncertainties, given in Table 2,
 474 are broadly consistent with a mini-Neptune sized
 475 planet ($3.82 \pm 0.16 R_\oplus$) on a close-in circular³
 476 orbit around a G8V host star ($0.88 \pm 0.02 R_\odot$). This
 477 best-fit planet size is consistent with those previ-
 478 ously reported by Morton et al. (2016) and Berger
 479 et al. (2018), and corrects for the small amount of
 480 flux dilution from Kepler 1627B.

4.1.2. Transit Asymmetry

481 The transit fit however is not perfect: the lower
 482 panels of Figure 5 show an asymmetric residual in

³ Our transit fitting yields $e < 0.48$ at 2σ ; the constraints on the eccentricity are not particularly strong.

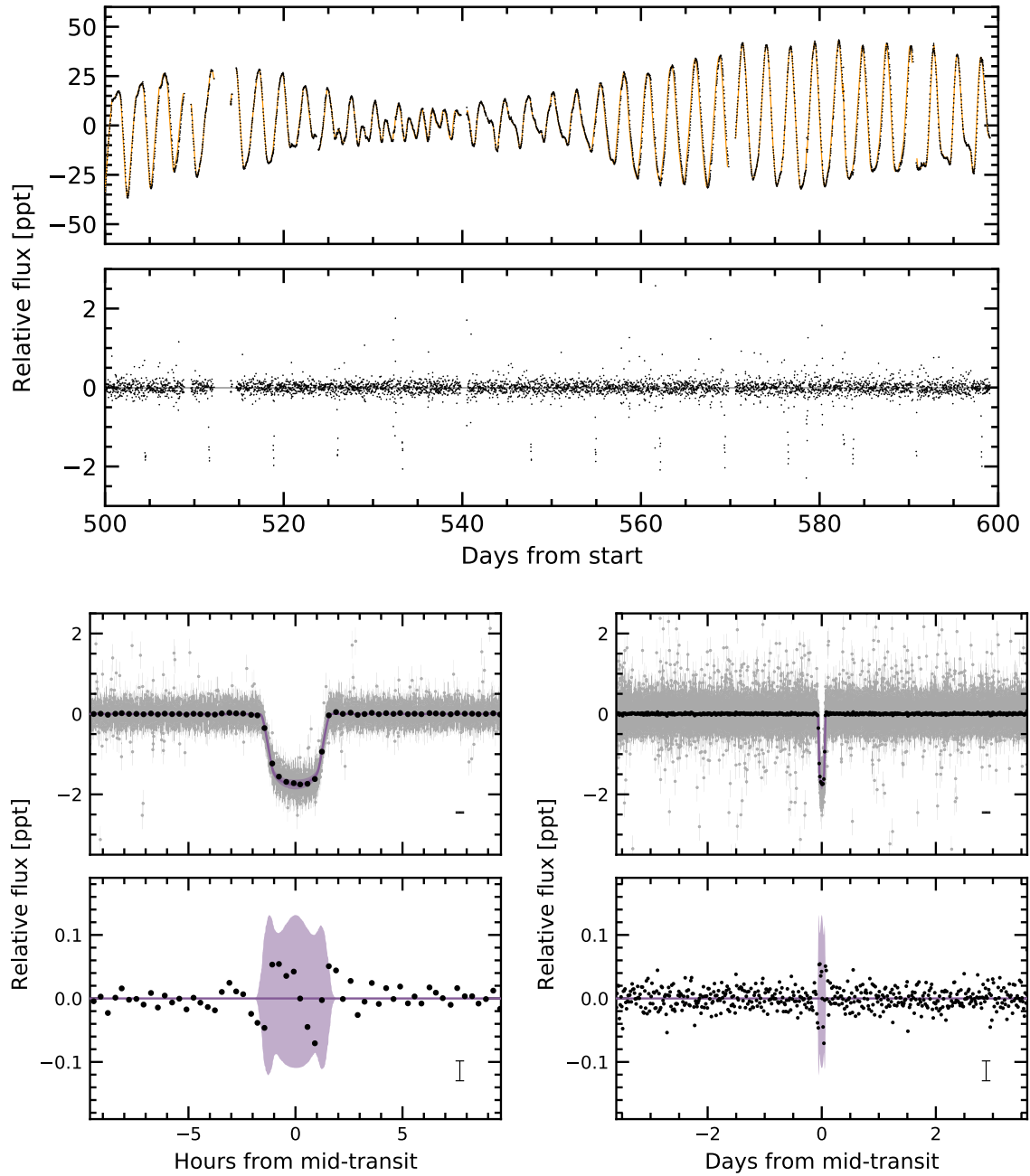


Figure 5. The light curve of Kepler 1627. *Top:* The Kepler data span 1,437 days (3.9 years), sampled at 30 minute cadence; a 100 day segment is shown. The top panel shows the PDCSAP median-subtracted flux in units of parts-per-thousand ($\times 10^{-3}$). The dominant signal is induced by starspots. The stellar variability model (orange line) is subtracted below, revealing the transits of Kepler 1627Ab. The online Figure Set spans the entire 3.9 years of observations. *Bottom:* Phase-folded transit of Kepler 1627Ab with stellar variability removed. Windows over 20 hours (*left*) and the entire orbit (*right*) are shown, and the residual after subtracting the transit is in the bottom-most row. The 2- σ model uncertainties and the best-fit model are the light purple band and the dark purple line. Gray points are individual flux measurements; black points bin these to 20 minute intervals, and have a representative 1- σ error bar in the lower right of each panel. The asymmetric residual during transit is larger than the out-of-transit scatter.

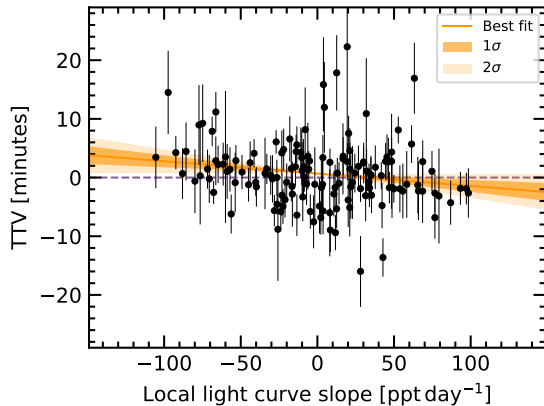


Figure 6. Possible evidence for a prograde orbit of Kepler 1627 Ab. The time of each Kepler transit was measured, along with the local slope of the light curve. The two quantities are weakly anti-correlated ($\approx 2\sigma$), which might be caused by starspot crossings during the first (second) half of transit inducing a positive (negative) TTV, provided that the orbit is prograde (Mazeh et al. 2015). The units along the abscissa can be understood by considering that the stellar flux changes by ~ 60 ppt per half rotation period (~ 1.3 days).

the data relative to the model: the measured flux is high during the first half of transit, and low in the second half. The semi-amplitude of this deviation is ≈ 50 ppm, which represents a $\approx 3\%$ distortion of the transit depth ($\delta = 1759 \pm 62$ ppm). Note that although this asymmetry is within the 2σ model uncertainties, the model has a jitter term that grows to account for excess white noise in the flux. The significance of the asymmetry is therefore best assessed in comparison against the intrinsic out-of-transit scatter in the data (≈ 16 ppm), not the model uncertainties. The lower right panel of Figure 5 demonstrates that the scatter during transit is higher than during all other phases of the planet’s orbit.

To determine whether the asymmetry could be a systematic caused by our stellar variability model, we explored an alternative approach in which we isolated each transit window, locally fitted out polynomial trends, and then binned all the observed transits; the asymmetry was still present at a comparable amplitude. Appendix B describes a more detailed analysis, which finds that the asymmetry also seems to be robust to different methods of data binning in time and by local light curve slope. Possible astrophysical explanations are discussed in Section 5.

4.1.3. Transit Timing and the Local Slope

The previous analysis by Holczer et al. (2016) did not find any significant long-term transit timing or duration variations (TTVs or TDVs) for

Kepler 1627. Quantitatively, the mean and standard deviation of the TTVs and TDVs they measured were -1.1 ± 13.8 min and -3.3 ± 22.1 min. In an earlier analysis however, Holczer et al. (2015) studied correlations between TTVs and local light curve slopes, and for Kepler 1627 found a weak correlation of -29 ± 13 min day $^{-1}$ between the two quantities. Given the possible connection between such correlations and the unresolved starspot crossings that we expect to be present in the Kepler 1627 light curve (Mazeh et al. 2015), we opted to re-examine the individual transit times.

We therefore isolated each of the 144 observed transits to within ± 4.5 hr of each transit, and fitted each window with both *i*) a local polynomial baseline plus the transit, and *ii*) a local linear trend. We considered the results both for a second and fourth-order time-dependence in the local baseline. We let the mid-time of each transit float, and then calculated the residual between the measured mid-time and that of a periodic orbit. This residual, the transit timing variation, is plotted in Figure 6 against the local linear slope for the fourth-order polynomial baseline. The slope of -21 ± 10 min day $^{-1}$ is similar to that found by Holczer et al. (2015).

One concern we had in this analysis was whether our transit fitting procedure might induce spurious correlations between the slope and transit time. In particular, using the second-order polynomial baseline yielded a larger anti-correlation between the TTVs and local slopes, of -79 ± 14 min day $^{-1}$. We therefore performed an injection-recovery procedure in which we injected transits at different phases in the Kepler 1627 light curve and repeated the TTV analysis. This was done at ≈ 50 phases, each separated by $0.02 P_{\text{orb}}$ while omitting the phases in transit. For the second-order polynomial baseline, this procedure yielded a similar anti-correlation in the injected transits as that present in the real transit; using this baseline would therefore bias the result. However for the fourth-order baseline, the correlation present in the data was stronger than in all but one of the injected transits. Possible interpretations are discussed below. Given the statistical significance, this analysis should be interpreted as suggestive at best.

4.2. Planet Confirmation

If the Kepler 1627Ab transit signal is created by a genuine planet, then to our knowledge it would be the youngest planet yet found by the main Kepler mission.⁴ Could the transit be produced by

⁴ The re-purposed K2 mission however has found two younger systems containing five planets: K2-33b (9 ± 1 Myr; Mann et al. 2016; David et al. 2016) and V1298 Tau (23 ± 4 Myr; David et al. 2019).

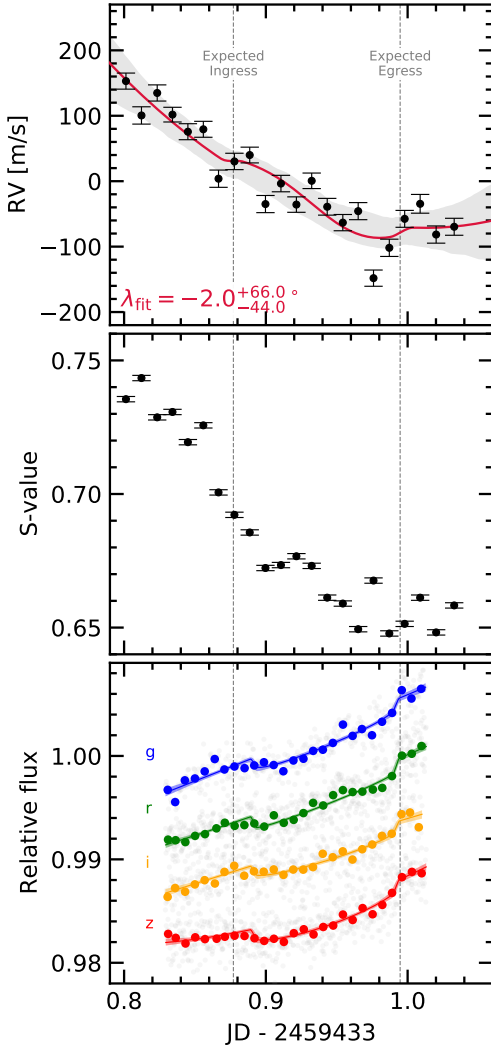


Figure 7. Keck/HIRES radial velocities and MuSCAT3 photometry from the transit of 2021 Aug 7. Top: The radial velocity jitter across the 15 minute exposures ($\sigma_{\text{RV}} \approx 30 \text{ m s}^{-1}$) prevented us from detecting the RM effect; a model including the RM anomaly and a quadratic trend in time to fit the spot-induced $\approx 250 \text{ m s}^{-1}$ trend is shown (see Appendix C). Shaded bands show $2-\sigma$ model uncertainties. Middle: The RV variations are strongly correlated with varying emission in the Ca H and K lines. Bottom: The photometric transit depths are consistent across the *griz* bandpasses. The photometry is binned at 10 minute intervals.

anything other than a planet orbiting this near-solar analog? Morton et al. (2016) validated the planet based on the transit shape, arguing that the most probable false positive scenario was that of a background eclipsing binary, which had a model-dependent probability of $\approx 10^{-5}$. However, this calculation was performed without knowledge of the low-mass stellar companion ($M_B \approx 0.33 M_\odot$). Validated planets have also previously been refuted

(e.g., Shporer et al. 2017). We therefore reassessed false positive scenarios in some detail.

As an initial plausibility check, Kepler 1627B contributes 1% to 2% of the total flux observed in the Kepler aperture. For the sake of argument, assume the former value. The observed transit has a depth of $\approx 0.18\%$. A 18% deep eclipse of Kepler 1627B would therefore be needed to produce a signal with the appropriate depth. The shape of the transit signal however requires the impact parameter to be below 0.77 ($2-\sigma$); the tertiary transiting the secondary would therefore need to be non-grazing with $R_3/R_2 \approx 0.4$. This yields a contradiction: this scenario requires an ingress and egress phase that each span $\approx 40\%$ of the transit duration (≈ 68 min). The actual measured ingress and egress duration is ≈ 17 min, a factor of four times too short. The combination of Kepler 1627B’s brightness, the transit depth, and the ingress duration therefore disfavor the scenario that Kepler 1627B might host the transit signal.

Beyond this simple test, a line of evidence that effectively confirms the planetary interpretation is that the stellar density implied by the transit duration and orbital period is inconsistent with an eclipsing body around the M-dwarf companion. We find $\rho_* = 2.00 \pm 0.24 \text{ g cm}^{-3}$, while the theoretically expected density for Kepler 1627B is $\approx 4.6 \text{ g cm}^{-3}$ (Table 2; Choi et al. 2016). The transit duration is therefore too long to be explained by a star eclipsing the M dwarf secondary at $10-\sigma$. While the planet might hypothetically still orbit a hidden close and bright companion, this possibility is implausible given *i*) the lack of secondary lines in the HIRES spectra, *ii*) the lack of secondary rotation signals in the Kepler photometry, and *iii*) the proximity of Kepler 1627 to the δ Lyr cluster locus on the Gaia CAMD (Figure 3).

The correlation noted in Section 4.1.3 between the TTVs and the local light curve slope might be an additional line of evidence in support of the planetary interpretation. Unless it is a statistical fluke (a $\approx 5\%$ possibility), then the most likely cause of the correlation is unresolved starspot crossings (Mazeh et al. 2015). These would only be possible if the planet transits the primary star, which excludes a background eclipsing binary scenario. The correlation would also suggest that the planet’s orbit is prograde. The latter point assumes that the dominant photometric variability is induced by dark spots, and not bright faculae. Given the observed transition of Sun-like stellar variability from spot to faculae-dominated regimes between young and old ages, we expect this latter assumption to be reasonably secure (Shapiro et al. 2016; Montet et al. 2017; Reinhold & Hekker 2020).

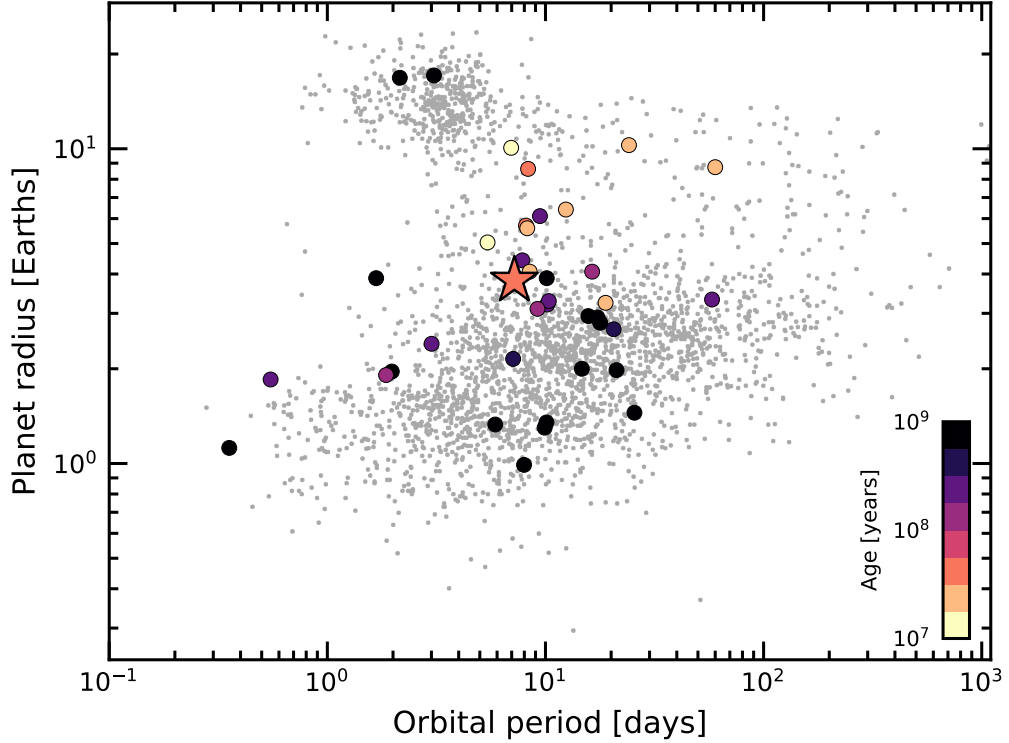


Figure 8. Radii, orbital periods, and ages of transiting exoplanets. Planets younger than a gigayear with $\tau/\sigma_\tau > 3$ are emphasized, where τ is the age and σ_τ is its uncertainty. Kepler 1627Ab is shown with a star. The large sizes of the youngest transiting planets could be explained by their primordial atmospheres not yet having evaporated; direct measurements of the atmospheric outflows or planetary masses would help to confirm this expectation. Selection effects may also be important. Parameters are from the NASA Exoplanet Archive (2021 Sept 15).

A third supporting line of evidence for the planetary interpretation also exists. We observed a transit of Kepler 1627Ab on the night of 2021 Aug 7 simultaneously with Keck/HIRES and MuSCAT3. We scheduled the observations using the ephemeris of Holczer et al. (2016). Although we did not detect the Rossiter-McLaughlin (RM) anomaly, the multi-band MuSCAT3 light curves show that the transit is achromatic (Figure 7). Quantitatively, when we fitted the MuSCAT3 photometry with a model that lets the transit depths vary across each bandpass, we found *griz* depths consistent with the Kepler depth at 0.6, 0.3, 0.3, and 1.1σ respectively. Conditioned on the ephemeris and transit depth from the Kepler data, the MuSCAT3 observations also suggested a transit duration 17.3 ± 4.3 min shorter than the Kepler transits. However, given both the lack of TDVs in the Kepler data and the relatively low signal-to-noise of the MuSCAT3 transit, further photometric follow-up would be necessary to determine whether the transit duration is indeed changing. For our RM analysis, the details are discussed in Appendix C. While the velocities are marginally more consistent with a prograde or polar orbit than a retrograde orbit, the spot-corrected exposure-to-exposure scat-

ter ($\sigma_{RV} \approx 30 \text{ m s}^{-1}$) is comparable to the expected RM anomaly assuming an aligned orbit ($\Delta v_{RM} \approx 20 \text{ m s}^{-1}$). We are therefore not in a position to claim a spectroscopic detection of the RM effect, nor to quantify the stellar obliquity.

5. DISCUSSION & CONCLUSIONS

Kepler 1627Ab provides a new extremum in the ages of the Kepler planets, and opens multiple avenues for further study. Observations of spectroscopic transits at greater precision should yield a measurement of the stellar obliquity, which would confirm or refute the prograde orbital geometry suggested by the TTV-local slope correlation. Separately, transit spectroscopy aimed at detecting atmospheric outflows could yield insight into the evolutionary state of the atmosphere (e.g., Ehrenreich et al. 2015; Spake et al. 2018; Vissapragada et al. 2020). Observations that quantify the amount of high-energy irradiation incident on the planet would complement these efforts, by helping to clarify the expected outflow rate (e.g., Poppenhaeger et al. 2021). Finally, a challenging but informative quantity to measure would be the planet's mass. Measured at sufficient precision, for instance through a multi-wavelength radial velocity campaign, the combination of the size, mass, and age

would yield constraints on both the planet's composition and its initial entropy (Owen 2020).

More immediately, the Kepler data may yet contain additional information. For instance, one possible explanation for the transit asymmetry shown in Figure 5 is that of a dusty asymmetric outflow. Dusty outflows are theoretically expected for young mini-Neptunes, and the amplitude of the observed asymmetry is consistent with predictions (Wang & Dai 2019). A second possibility is that the planetary orbit is slightly misaligned from the stellar spin axis, and tends to transit starspot groups at favored stellar latitudes. This geometry would be necessary in order to explain how the starspot crossings could add up coherently. Other possibilities including gravity darkening or TTVs causing the asymmetry are disfavored (see Appendix B).

Beyond the asymmetric transits, Appendix D highlights an additional abnormality in the short-cadence Kepler data, in the arrival time distribution of stellar flares. We encourage its exploration by investigators more versed in the topic than ourselves.

In the context of the transiting planet population, Kepler 1627Ab is among the youngest known (Figure 8). Comparable systems with precise ages include K2-33 (Mann et al. 2016; David et al. 2016), DS Tuc (Benatti et al. 2019; Newton et al. 2019), HIP 67522 (Rizzuto et al. 2020), TOI 837 (Bouma et al. 2020), the two-planet AU Mic (Plavchan et al. 2020; Martioli et al. 2021) and the four-planet V1298 Tau (David et al. 2019). Kepler 1627Ab is one of the smaller planets in this sample ($3.82 \pm 0.16 R_{\oplus}$), which could be linked to the selection effects imposed by spot-induced photometric variability at very young ages (e.g., Zhou et al. 2021). However, smaller planets could have been detected: the Kepler pipeline's median completeness extended to $1.6 R_{\oplus}$ at 10 day orbital periods, and $3.3 R_{\oplus}$ at 100 days (Burke & Catanzarite 2021). The large size of Kepler 1627Ab relative to most Kepler mini-Neptunes might therefore support a picture in which the typical $5 M_{\oplus}$ to $10 M_{\oplus}$ mini-Neptune (Wu 2019) loses a significant fraction of its primordial atmosphere over its first gigayear (Owen & Wu 2013; Ginzburg et al. 2018).

Ultimately, the main advance of this work is a precise measurement of the age of Kepler 1627Ab. This measurement was enabled by identifying the connection of the star to the δ Lyr cluster using Gaia kinematics, and by then using the Gaia color-absolute magnitude diagram and TESS stellar rotation periods to verify the cluster's existence. Table 3 enables similar cross-matches for both known and forthcoming exoplanet systems (e.g., Guerrero et al. 2021). Confirming these candidate associations using independent age indicators is essential

because their false positive rates are not known. A related path is to identify new kinematic associations around known exoplanet host stars using positions and tangential velocities from Gaia, and to verify these associations with stellar rotation periods and spectroscopy (e.g., Tofflemire et al. 2021). Each approach seems likely to expand the census of planets with precisely measured ages over the coming years, which will help in deciphering the early stages of exoplanet evolution.

ACKNOWLEDGMENTS

The authors are grateful to J. Winn, J. Spake, A. Howard, and T. David for illuminating discussions and suggestions, and to R. Kerr for providing us with the Kerr et al. (2021) membership list prior to its publication. The authors are also grateful to K. Collins for helping resolve the scheduling conflict that would have otherwise prevented the MuSCAT3 observations. L.G.B. acknowledges support from a Charlotte Elizabeth Procter Fellowship from Princeton University, as well as from the TESS GI Program (NASA grants 80NSSC19K0386 and 80NSSC19K1728) and the Heising-Simons Foundation (51 Pegasi b Fellowship). Keck/NIRC2 imaging was acquired by program 2015A/N301N2L (PI: A. Kraus). In addition, this paper is based in part on observations made with the MuSCAT3 instrument, developed by the Astrobiology Center and under financial support by JSPS KAKENHI (JP18H05439) and JST PRESTO (JPMJPR1775), at Faulkes Telescope North on Maui, HI, operated by the Las Cumbres Observatory. This work is partly supported by JSPS KAKENHI Grant Numbers 22000005, JP15H02063, JP17H04574, JP18H05439, JP18H05442, JST PRESTO Grant Number JPMJPR1775, the Astrobiology Center of National Institutes of Natural Sciences (NINS) (Grant Number AB031010). This paper also includes data collected by the TESS mission, which are publicly available from the Mikulski Archive for Space Telescopes (MAST). Funding for the TESS mission is provided by NASA's Science Mission directorate. We thank the TESS Architects (G. Ricker, R. Vandervort, D. Latham, S. Seager, J. Jenkins) and the many TESS team members for their efforts to make the mission a continued success. Finally, this research has made use of the Keck Observatory Archive (KOA), which is operated by the W. M. Keck Observatory and the NASA Exoplanet Science Institute (NExScI), under contract with the National Aeronautics and Space Administration. We also thank the Keck Observatory staff for their support of HIRES and remote observing. We recognize

797 the importance that the summit of Maunakea has
798 within the indigenous Hawaiian community, and
799 are deeply grateful to have the opportunity to con-
800 duct observations from this mountain.

801 *Software:* altaipony (Ilin et al. 2021),
802 astrobase (Bhatti et al. 2018), astropy (As-
803 tropy Collaboration et al. 2018), astroquery
804 (Ginsburg et al. 2018), corner (Foreman-Mackey
805 2016), exoplanet (Foreman-Mackey et al.
806 2020), and its dependencies (Agol et al. 2020; Kip-
807 ping 2013; Luger et al. 2019; Theano Develop-
808 ment Team 2016), PyMC3 (Salvatier et al. 2016),
809 scipy (Jones et al. 2001), TESS-point (Burke
810 et al. 2020), wotan (Hippke et al. 2019).

811 *Facilities:* Astrometry: Gaia (Gaia Col-
812 laboration et al. 2018b, 2021a). Imaging:
813 Second Generation Digitized Sky Survey.
814 Keck:II (NIRC2; [www2.keck.hawaii.edu/inst/
nirc2](http://www2.keck.hawaii.edu/inst/nirc2)). Gemini:North ('Alopeke; Scott et al. 2018,
815 2021). Spectroscopy: Keck:I (HIRES; Vogt et al.
816 1994). Photometry: Kepler (Borucki et al. 2010),
817 MuSCAT3 (Narita et al. 2020), TESS (Ricker et al.
818 2015).

Table 1. Literature and Measured Properties for Kepler 1627

Primary Star			
TIC 120105470 GAIADR2 [†] 2103737241426734336			
Parameter	Description	Value	Source
$\alpha_{J2015.5}$	Right Ascension (hh:mm:ss)	18:56:13.6	1
$\delta_{J2015.5}$	Declination (dd:mm:ss)	+41:34:36.22	1
V	Johnson V mag.	13.11 \pm 0.08	2
G	Gaia G mag.	13.02 \pm 0.02	1
G_{BP}	Gaia BP mag.	13.43 \pm 0.02	1
G_{RP}	Gaia RP mag.	12.44 \pm 0.02	1
T	TESS T mag.	12.53 \pm 0.02	2
J	2MASS J mag.	11.69 \pm 0.02	3
H	2MASS H mag.	11.30 \pm 0.02	3
K _S	2MASS K _S mag.	11.19 \pm 0.02	3
π	Gaia EDR3 parallax (mas)	3.009 \pm 0.032	1
d	Distance (pc)	329.5 \pm 3.5	1, 4
μ_α	Gaia EDR3 proper motion	1.716 \pm 0.034	1
	in RA (mas yr ⁻¹)		
μ_δ	Gaia EDR3 proper motion	-1.315 \pm 0.034	1
	in DEC (mas yr ⁻¹)		
RUWE	Gaia EDR3 renormalized	2.899	1
	unit weight error		
RV	Systemic radial velocity (km s ⁻¹)	-16.7 \pm 1.0	5
Spec. Type	Spectral Type	G8V	5
$v \sin i_*$	Rotational velocity* (km s ⁻¹)	18.9 \pm 1.0	5
Li EW	6708Å Equiv. Width (mÅ)	235 ⁺⁵ ₋₇	5
T_{eff}	Effective Temperature (K)	5505 \pm 60	6
$\log g_*$	Surface Gravity (cgs)	4.53 \pm 0.05	6
R_*	Stellar radius (R_\odot)	0.881 \pm 0.018	6
M_*	Stellar mass (R_\odot)	0.953 \pm 0.019	6
Av	Interstellar reddening (mag)	0.2 \pm 0.1	6
[Fe/H]	Metallicity	0.1 \pm 0.1	6
P_{rot}	Rotation period (d)	2.642 \pm 0.042	7
Age	Adopted stellar age (Myr)	38 ⁺⁶ ₋₅	8
Δm_{832}	Mag difference ('Alopeke 832 nm)	3.14 \pm 0.15	9
θ_B	Position angle (deg)	92 \pm 1	9
ρ_B	Apparent separation of	0.164 \pm 0.002	9
	primary and secondary (as)		
ρ_B	Apparent separation of	53 \pm 4	1, 4, 9
	primary and secondary (AU)		
$\Delta m_{K'}$	Mag difference (NIRC2 K')	2.37 \pm 0.02	10
θ_B	Position angle (deg)	95.9 \pm 0.5	10
ρ_B	Apparent separation of	0.1739 \pm 0.0010	10
	primary and secondary (as)		

NOTE—[†] The GAIADR2 and GAIAEDR3 identifiers for Kepler 1627A are identical. The secondary is not resolved in the Gaia point source catalog. * Given only $v \sin i$ and $2\pi R_*/P_{\text{rot}}$, $\cos i = 0.11_{-0.08}^{+0.11}$. Provenances are: ¹Gaia Collaboration et al. (2021a), ²Stassun et al. (2019), ³Skrutskie et al. (2006), ⁴Lindgren et al. (2021), ⁵HIREs spectra and Yee et al. (2017), ⁶Cluster isochrone (MIST adopted; PARSEC compared for quoted uncertainty), ⁷Kepler light curve, ⁸Pre-main-sequence CAMD interpolation (Section 2.2.1), ⁹'Alopeke imaging 2021 June 24 (Scott et al. 2021), ¹⁰NIRC2 imaging 2015 July 22, using the Yelda et al. (2010) optical distortion solution to convert pixel-space relative positions to on-sky relative astrometry. The “discrepancy” between the two imaging epochs likely indicates orbital motion.

Table 2. Priors and Posteriors for Model Fitted to the Long Cadence Kepler 1627Ab Light Curve.

Param.	Unit	Prior	Median	Mean	Std. Dev.	3%	97%	ESS	$\hat{R} - 1$
<i>Sampled</i>									
P	d	$\mathcal{N}(7.20281; 0.01000)$	7.2028038	7.2028038	0.0000073	7.2027895	7.2028168	7464	3.9e-04
$t_0^{(1)}$	d	$\mathcal{N}(120.79053; 0.02000)$	120.7904317	120.7904254	0.0009570	120.7886377	120.7921911	3880	2.0e-03
$\log \delta$	—	$\mathcal{N}(-6.3200; 2.0000)$	-6.3430	-6.3434	0.0354	-6.4094	-6.2767	6457	3.0e-04
$b^{(2)}$	—	$\mathcal{U}(0.000; 1.000)$	0.4669	0.4442	0.2025	0.0662	0.8133	1154	1.6e-03
u_1	—	Kipping (2013)	0.271	0.294	0.190	0.000	0.628	3604	1.5e-03
u_2	—	Kipping (2013)	0.414	0.377	0.326	-0.240	0.902	3209	1.4e-03
R_*	R_{\odot}	$\mathcal{N}(0.881; 0.018)$	0.881	0.881	0.018	0.847	0.915	8977	3.1e-04
$\log g$	cgs	$\mathcal{N}(4.530; 0.050)$	4.532	4.533	0.051	4.435	4.627	6844	1.6e-03
$\langle f \rangle$	—	$\mathcal{N}(0.000; 0.100)$	-0.0003	-0.0003	0.0001	-0.0005	-0.0000	8328	1.1e-03
$e^{(3)}$	—	Van Eylen et al. (2019)	0.154	0.186	0.152	0.000	0.459	1867	2.0e-03
ω	rad	$\mathcal{U}(0.000; 6.283)$	0.055	0.029	1.845	-3.139	2.850	3557	8.6e-05
$\log \sigma_f$	—	$\mathcal{N}(\log \langle \sigma_f \rangle; 2.000)$	-8.035	-8.035	0.008	-8.049	-8.021	9590	3.9e-04
σ_{rot}	d^{-1}	InvGamma(1.000; 5.000)	0.070	0.070	0.001	0.068	0.072	9419	1.4e-03
$\log P_{\text{rot}}$	log(d)	$\mathcal{N}(0.958; 0.020)$	0.978	0.978	0.001	0.975	0.980	8320	2.2e-04
$\log Q_0$	—	$\mathcal{N}(0.000; 2.000)$	-0.327	-0.326	0.043	-0.407	-0.246	9659	2.7e-04
$\log dQ$	—	$\mathcal{N}(0.000; 2.000)$	7.697	7.698	0.103	7.511	7.899	5824	3.7e-04
f	—	$\mathcal{U}(0.010; 1.000)$	0.01006	0.01009	0.00009	0.01000	0.01025	4645	4.0e-04
<i>Derived</i>									
δ	—	—	0.001759	0.001759	0.000062	0.001641	0.001875	6457	3.0e-04
R_p/R_*	—	—	0.039	0.039	0.001	0.037	0.042	1811	1.1e-03
ρ_*	g cm^{-3}	—	1.990	2.004	0.240	1.570	2.461	6905	2.1e-03
$R_p^{(4)}$	R_{Jup}	—	0.337	0.338	0.014	0.314	0.367	2311	1.0e-03
$R_p^{(4)}$	R_{Earth}	—	3.777	3.789	0.157	3.52	4.114	2311	1.0e-03
a/R_*	—	—	17.606	17.619	0.702	16.277	18.906	6905	2.1e-03
$\cos i$	—	—	0.027	0.025	0.010	0.004	0.040	1312	1.2e-03
T_{14}	hr	—	2.841	2.843	0.060	2.734	2.958	3199	3.6e-04
T_{13}	hr	—	2.555	2.539	0.094	2.360	2.692	1960	1.4e-03

NOTE— ESS refers to the number of effective samples. \hat{R} is the Gelman-Rubin convergence diagnostic. Logarithms in this table are base-e. \mathcal{U} denotes a uniform distribution, and \mathcal{N} a normal distribution. (1) The ephemeris is in units of BJDTDB - 2454833. (2) Although $\mathcal{U}(0, 1 + R_p/R_*)$ is formally correct, for this model we assumed a non-grazing transit to enable sampling in $\log \delta$. (3) The eccentricity vectors are sampled in the $(e \cos \omega, e \sin \omega)$ plane. (4) The true planet size is a factor of $((F_1 + F_2)/F_1)^{1/2}$ larger than that from the fit because of dilution from Kepler 1627B, where F_1 is the flux from the primary, and F_2 is that from the secondary; the mean and standard deviation of $R_p = 3.817 \pm 0.158 R_{\oplus}$ quoted in the text includes this correction, assuming $(F_1 + F_2)/F_1 \approx 1.015$.

Table 3. Young, Age-dated, and Age-dateable Stars Within the Nearest Few Kiloparsecs.

Parameter	Example Value	Description
source_id	1709456705329541504	Gaia DR2 source identifier.
ra	247.826	Gaia DR2 right ascension [deg].
dec	79.789	Gaia DR2 declination [deg].
parallax	35.345	Gaia DR2 parallax [mas].
parallax_error	0.028	Gaia DR2 parallax uncertainty [mas].
pmra	94.884	Gaia DR2 proper motion $\mu_{\alpha} \cos \delta$ [mas yr $^{-1}$].
pmdec	-86.971	Gaia DR2 proper motion μ_{δ} [mas yr $^{-1}$].
phot_g_mean_mag	6.85	Gaia DR2 G magnitude.
phot_bp_mean_mag	6.409	Gaia DR2 G_{BP} magnitude.
phot_rp_mean_mag	7.189	Gaia DR2 G_{RP} magnitude.
cluster	NASAExoArchive_ps_20210506.Uma,IR_excess	Comma-separated cluster or group name.
age	9.48,nan,nan	Comma-separated logarithm (base-10) of reported ^a age in years.
mean_age	9.48	Mean (ignoring NaNs) of age column.
reference_id	NASAExoArchive_ps_20210506,Ujjwal2020,CottenSong2016	Comma-separated provenance of group membership.
reference_bibcode	2013PASP..125..989A,2020AJ....159..166U,2016ApJS..225..15C	ADS bibcode corresponding to reference_id.

NOTE— Table 3 is published in its entirety in a machine-readable format. This table is a concatenation of the studies listed in Table 4. One entry is shown for guidance regarding form and content. In this particular example, the star has a cold Jupiter on a 16 year orbit, HD 150706b (Boisse et al. 2012). An infrared excess has been reported (Cotten & Song 2016), and the star was identified by Ujjwal et al. (2020) as a candidate UMa moving group member (≈ 400 Myr; Mann et al. 2020). The star's RV activity and TESS rotation period corroborate its youth.

Table 4. Provenances of Young and Age-dateable Stars.

Reference	N_{Gaia}	N_{Age}	$N_{G_{\text{RP}} < 16}$
Kounkel et al. (2020)	987376	987376	775363
Cantat-Gaudin & Anders (2020)	433669	412671	269566
Cantat-Gaudin et al. (2018)	399654	381837	246067
Kounkel & Covey (2019)	288370	288370	229506
Cantat-Gaudin et al. (2020)	233369	227370	183974
Zari et al. (2018) UMS	86102	0	86102
Wenger et al. (2000) Y*?	61432	0	45076
Zari et al. (2018) PMS	43719	0	38435
Gaia Collaboration et al. (2018a) $d > 250 \text{ pc}$	35506	31182	18830
Castro-Ginard et al. (2020)	33635	24834	31662
Kerr et al. (2021)	30518	25324	27307
Wenger et al. (2000) Y*○	28406	0	16205
Villa Vélez et al. (2018)	14459	14459	13866
Cantat-Gaudin et al. (2019)	11843	11843	9246
Damiani et al. (2019) PMS	10839	10839	9901
Oh et al. (2017)	10379	0	10370
Meingast et al. (2021)	7925	7925	5878
Wenger et al. (2000) pMS*	5901	0	3006
Gaia Collaboration et al. (2018a) $d < 250 \text{ pc}$	5378	817	3968
Kounkel et al. (2018)	5207	3740	5207
Ratzenböck et al. (2020)	4269	4269	2662
Wenger et al. (2000) TT*	4022	0	3344
Damiani et al. (2019) UMS	3598	3598	3598
Rizzuto et al. (2017)	3294	3294	2757
Akeson et al. (2013)	3107	868	3098
Tian (2020)	1989	1989	1394
Goldman et al. (2018)	1844	1844	1783
Cotten & Song (2016)	1695	0	1693
Gagné et al. (2018b)	1429	0	1389
Röser & Schilbach (2020) Psc-Eri	1387	1387	1107
Röser & Schilbach (2020) Pleiades	1245	1245	1019
Wenger et al. (2000) TT?	1198	0	853
Gagné & Faherty (2018)	914	0	913
Pavlidou et al. (2021)	913	913	504
Gagné et al. (2018a)	692	0	692
Ujjwal et al. (2020)	563	0	563
Gagné et al. (2020)	566	566	351
Esplin & Luhman (2019)	377	443	296
Roccatagliata et al. (2020)	283	283	232
Meingast & Alves (2019)	238	238	238
Fürnkranz et al. (2019) Coma-Ber	214	214	213
Fürnkranz et al. (2019) Neighbor Group	177	177	167
Kraus et al. (2014)	145	145	145

NOTE— Table 4 describes the provenances for the young and age-dateable stars in Table 3. N_{Gaia} : number of Gaia stars we parsed from the literature source. N_{Age} : number of stars in the literature source with ages reported. $N_{G_{\text{RP}} < 16}$: number of Gaia stars we parsed from the literature source with either $G_{\text{RP}} < 16$, or a parallax S/N exceeding 5 and a distance closer than 100 pc. The latter criterion included a few hundred white dwarfs that would have otherwise been neglected. Some studies are listed multiple times if they contain multiple tables. Wenger et al. (2000) refers to the SIMBAD database.

REFERENCES

- 820 Agol, E., Luger, R., & Foreman-Mackey, D. 2020, *AJ*,
 821 159, 123
- 822 Akeson, R. L., Chen, X., Ciardi, D., et al. 2013, *PASP*,
 823 125, 989
- 824 Astropy Collaboration, Price-Whelan, A. M., Sipőcz,
 825 B. M., et al. 2018, *AJ*, 156, 123
- 826 Baraffe, I., Homeier, D., Allard, F., & Chabrier, G.
 827 2015, *A&A*, 577, A42
- 828 Beaumont, C., Robitaille, T., Borkin, M., & Goodman,
 829 A. 2014, glueviz v0.4: multidimensional data
 830 exploration
- 831 Benatti, S., Nardiello, D., Malavolta, L., et al. 2019,
 832 *A&A*, 630, A81
- 833 Berger, T. A., Howard, A. W., & Boesgaard, A. M.
 834 2018, *ApJ*, 855, 115
- 835 Berger, T. A., Huber, D., Gaidos, E., & van Saders, J. L.
 836 2018, *ApJ*, 866, 99
- 837 Bhatti, W., Bouma, L. G., & Wallace, J. 2018,
 838 astrobase,
<https://doi.org/10.5281/zenodo.1469822>
- 840 Boisse, I., Pepe, F., Perrier, C., et al. 2012, *A&A*, 545,
 841 A55
- 842 Borucki, W. J., Koch, D., Basri, G., et al. 2010, *Science*,
 843 327, 977
- 844 Bossini, D., Vallenari, A., Bragaglia, A., et al. 2019,
 845 *A&A*, 623, A108
- 846 Bouma, L. G., Curtis, J. L., Hartman, J. D., Winn, J. N.,
 847 & Bakos, G. A. 2021, arXiv:2107.08050 [astro-ph]
- 848 Bouma, L. G., Hartman, J. D., Bhatti, W., Winn, J. N.,
 849 & Bakos, G. Á. 2019, *ApJS*, 245, 13
- 850 Bouma, L. G., Hartman, J. D., Brahm, R., et al. 2020,
 851 *AJ*, 160, 239
- 852 Bressan, A., Marigo, P., Girardi, L., et al. 2012,
 853 *MNRAS*, 427, 127
- 854 Burke, C., & Catanzarite, J. 2021, KeplerPORTS:
 855 Kepler Planet Occurrence Rate Tools
- 856 Burke, C. J., Levine, A., Fausnaugh, M., et al. 2020,
 857 TESS-Point: High precision TESS pointing tool,
 858 Astrophysics Source Code Library, ascl:2003.001
- 859 Cantat-Gaudin, T., & Anders, F. 2020, *A&A*, 633, A99
- 860 Cantat-Gaudin, T., Jordi, C., Vallenari, A., et al. 2018,
 861 *A&A*, 618, A93
- 862 Cantat-Gaudin, T., Jordi, C., Wright, N. J., et al. 2019,
 863 *A&A*, 626, A17
- 864 Cantat-Gaudin, T., Anders, F., Castro-Ginard, A., et al.
 865 2020, *A&A*, 640, A1
- 866 Capitanio, L., Lallement, R., Vergely, J. L., Elyajouri,
 867 M., & Monreal-Ibero, A. 2017, *A&A*, 606, A65
- 868 Castro-Ginard, A., Jordi, C., Luri, X., et al. 2020, *A&A*,
 869 635, A45
- 870 Choi, J., Dotter, A., Conroy, C., et al. 2016, *ApJ*, 823,
 871 102
- 872 Claret, A., & Bloemen, S. 2011, *A&A*, 529, A75
- 873 Cotten, T. H., & Song, I. 2016, *ApJS*, 225, 15
- 874 Dahm, S. E. 2015, *ApJ*, 813, 108
- 875 Dai, F., Winn, J. N., Berta-Thompson, Z.,
 876 Sanchis-Ojeda, R., & Albrecht, S. 2018, *AJ*, 155, 177
- 877 Damiani, F., Prisinzano, L., Pillitteri, I., Micela, G., &
 878 Sciortino, S. 2019, *A&A*, 623, A112
- 879 Davenport, J. R. A. 2016, *ApJ*, 829, 23
- 880 Davenport, J. R. A., Hawley, S. L., Hebb, L., et al.
 881 2014, *ApJ*, 797, 122
- 882 David, T., Hillenbrand, L., & Petigura, E. 2016, *Nature*,
 883 534, 658
- 884 David, T. J., & Hillenbrand, L. A. 2015, *ApJ*, 804, 146
- 885 David, T. J., Petigura, E. A., Luger, R., et al. 2019,
 886 *ApJL*, 885, L12
- 887 David, T. J., Contardo, G., Sandoval, A., et al. 2021, *AJ*,
 888 161, 265
- 889 Dias, W. S., Monteiro, H., Caetano, T. C., et al. 2014,
 890 *A&A*, 564, A79
- 891 Dobbie, P. D., Lodieu, N., & Sharp, R. G. 2010,
 892 *MNRAS*, 409, 1002
- 893 Douglas, S. T., Agüeros, M. A., Covey, K. R., & Kraus,
 894 A. 2017, *ApJ*, 842, 83
- 895 Douglas, S. T., Pérez Chávez, J., Cargile, P. A., et al.
 896 2021, Constraining Stellar Rotation at the ZAMS
- 897 Eggen, O. J. 1968, *ApJ*, 152, 77
- 898 Ehrenreich, D., Bourrier, V., Wheatley, P. J., et al. 2015,
 899 *Nature*, 522, 459
- 900 Esplin, T. L., & Luhman, K. L. 2019, *AJ*, 158, 54
- 901 Feinstein, A. D., Montet, B. T., Johnson, M. C., et al.
 902 2021, arXiv:2107.01213 [astro-ph]
- 903 Foreman-Mackey, D. 2016, *Journal of Open Source
 904 Software*, 1, 24
- 905 Foreman-Mackey, D., Czekala, I., Luger, R., et al. 2020,
 906 exoplanet-dev/exoplanet v0.2.6
- 907 Fulton, B. J., Petigura, E. A., Howard, A. W., et al.
 908 2017, *AJ*, 154, 109
- 909 Fürnkranz, V., Meingast, S., & Alves, J. 2019, *A&A*,
 910 624, L11
- 911 Gagné, J., David, T. J., Mamajek, E. E., et al. 2020,
 912 *ApJ*, 903, 96
- 913 Gagné, J., & Faherty, J. K. 2018, *ApJ*, 862, 138
- 914 Gagné, J., Roy-Loubier, O., Faherty, J. K., Doyon, R.,
 915 & Malo, L. 2018a, *ApJ*, 860, 43

- 916 Gagné, J., Mamajek, E. E., Malo, L., et al. 2018b, *ApJ*,
917 856, 23
- 918 Gagné, J., David, T. J., Mamajek, E. E., et al. 2020,
919 *ApJ*, 903, 96
- 920 Gaia Collaboration, Babusiaux, C., van Leeuwen, F.,
921 et al. 2018a, *A&A*, 616, A10
- 922 Gaia Collaboration, Brown, A. G. A., Vallenari, A.,
923 et al. 2018b, *A&A*, 616, A1
- 924 —. 2021a, *A&A*, 649, A1
- 925 Gaia Collaboration, Smart, R. L., Sarro, L. M., et al.
926 2021b, *A&A*, 649, A6
- 927 Gelman, A., & Rubin, D. B. 1992, *Statistical Science*, 7,
928 457, publisher: Institute of Mathematical Statistics
- 929 Gibson, S. R., Howard, A. W., Marcy, G. W., et al. 2016,
930 in *SPIE Conference Series*, Vol. 9908, *Ground-based*
931 and *Airborne Instrumentation for Astronomy VI*, ed.
932 C. J. Evans, L. Simard, & H. Takami, 990870
- 933 Gillen, E., Briegal, J. T., Hodgkin, S. T., et al. 2020,
934 *MNRAS*, 492, 1008
- 935 Ginsburg, A., Sipocz, B., Madhura Parikh, et al. 2018,
936 *Astropy/Astroquery: V0.3.7 Release*
- 937 Ginzburg, S., Schlichting, H. E., & Sari, R. 2018,
938 *MNRAS*, 476, 759
- 939 Goldman, B., Röser, S., Schilbach, E., Moór, A. C., &
940 Henning, T. 2018, *ApJ*, 868, 32
- 941 Guerrero, N. M., Seager, S., Huang, C. X., et al. 2021,
942 *ApJS*, 254, 39
- 943 Günther, M. N., Zhan, Z., Seager, S., et al. 2020, *AJ*,
944 159, 60
- 945 Hattori, S., Foreman-Mackey, D., Hogg, D. W., et al.
946 2021, arXiv e-prints, arXiv:2106.15063
- 947 Hippke, M., David, T. J., Mulders, G. D., & Heller, R.
948 2019, *AJ*, 158, 143
- 949 Hirano, T., Suto, Y., Taruya, A., et al. 2010, *ApJ*, 709,
950 458
- 951 Hirano, T., Suto, Y., Winn, J. N., et al. 2011, *ApJ*, 742,
952 69
- 953 Hoffman, M. D., & Gelman, A. 2014, *Journal of
954 Machine Learning Research*, 15, 1593
- 955 Holczer, T., Shporer, A., Mazeh, T., et al. 2015, *ApJ*,
956 807, 170
- 957 Holczer, T., Mazeh, T., Nachmani, G., et al. 2016,
958 *ApJS*, 225, 9
- 959 Howard, A. W., Johnson, J. A., Marcy, G. W., et al.
960 2010, *ApJ*, 721, 1467
- 961 Howell, S. B., Everett, M. E., Sherry, W., Horch, E., &
962 Ciardi, D. R. 2011, *AJ*, 142, 19
- 963 Ikoma, M., & Hori, Y. 2012, *ApJ*, 753, 66
- 964 Ilin, E., Schmidt, S. J., Poppenhöger, K., et al. 2021,
965 *A&A*, 645, A42
- 966 Jones, E., Oliphant, T., Peterson, P., et al. 2001, Open
967 source scientific tools for Python
- 968 Kerr, R. M. P., Rizzato, A. C., Kraus, A. L., & Offner,
969 S. S. R. 2021, *ApJ*, 917, 23
- 970 Kharchenko, N. V., Piskunov, A. E., Schilbach, E.,
971 Röser, S., & Scholz, R.-D. 2013, *A&A*, 558, A53
- 972 Kipping, D. M. 2010, *MNRAS*, 408, 1758
- 973 Kipping, D. M. 2013, *MNRAS*, 435, 2152
- 974 Kite, E. S., Fegley, Jr., B., Schaefer, L., & Ford, E. B.
975 2020, *ApJ*, 891, 111
- 976 Klein, B., & Donati, J.-F. 2020, *MNRAS*, 493, L92
- 977 Kounkel, M., & Covey, K. 2019, *AJ*, 158, 122
- 978 Kounkel, M., Covey, K., & Stassun, K. G. 2020, *AJ*,
979 160, 279
- 980 Kounkel, M., Covey, K., Suárez, G., et al. 2018, *AJ*,
981 156, 84
- 982 Kounkel, M., Covey, K., Suárez, G., et al. 2018, *AJ*,
983 156, 84
- 984 Kraus, A. L., Ireland, M. J., Huber, D., Mann, A. W., &
985 Dupuy, T. J. 2016, *AJ*, 152, 8
- 986 Kraus, A. L., Shkolnik, E. L., Allers, K. N., & Liu,
987 M. C. 2014, *AJ*, 147, 146
- 988 Lallement, R., Capitanio, L., Ruiz-Dern, L., et al. 2018,
989 *A&A*, 616, A132
- 990 Lindegren, L., Bastian, U., Biermann, M., et al. 2021,
991 *A&A*, 649, A4
- 992 Lomb, N. R. 1976, *Astrophysics and Space Science*, 39,
993 447
- 994 Luger, R., Agol, E., Foreman-Mackey, D., et al. 2019,
995 *AJ*, 157, 64
- 996 Mann, A. W., Newton, E. R., Rizzato, A. C., et al. 2016,
997 *AJ*, 152, 61
- 998 Mann, A. W., Johnson, M. C., Vanderburg, A., et al.
999 2020, *AJ*, 160, 179
- 1000 Martioli, E., Hébrard, G., Correia, A. C. M., Laskar, J.,
1001 & Lecavelier des Etangs, A. 2021, *A&A*, 649, A177
- 1002 Masuda, K. 2015, *ApJ*, 805, 28
- 1003 Mazeh, T., Holczer, T., & Shporer, A. 2015, *ApJ*, 800,
1004 142
- 1005 McCann, J., Murray-Clay, R. A., Kratter, K., &
1006 Krumholz, M. R. 2019, *ApJ*, 873, 89
- 1007 McKinney, W. 2010, in *Proceedings of the 9th Python
1008 in Science Conference*, ed. S. van der Walt &
1009 J. Millman, 51
- 1010 McQuillan, A., Mazeh, T., & Aigrain, S. 2014, *ApJS*,
1011 211, 24
- 1012 Meibom, S., Mathieu, R. D., & Stassun, K. G. 2007,
1013 *ApJL*, 665, L155
- 1014 Meibom, S., Barnes, S. A., Latham, D. W., et al. 2011,
1015 *ApJL*, 733, L9

- 1016 Meibom, S., Torres, G., Fressin, F., et al. 2013, *Nature*,
1017 499, 55
- 1018 Meingast, S., & Alves, J. 2019, *A&A*, 621, L3
- 1019 Meingast, S., Alves, J., & Rottensteiner, A. 2021, *A&A*,
1020 645, A84
- 1021 Montet, B. T., Tovar, G., & Foreman-Mackey, D. 2017,
1022 *ApJ*, 851, 116
- 1023 Montet, B. T., Feinstein, A. D., Luger, R., et al. 2020,
1024 *AJ*, 159, 112
- 1025 Morris, B. M. 2020, *ApJ*, 893, 67
- 1026 Morton, T. D., Bryson, S. T., Coughlin, J. L., et al.
1027 2016, *ApJ*, 822, 86
- 1028 Narita, N., Fukui, A., Yamamuro, T., et al. 2020, in
1029 *SPIE Conference Series*, 114475K
- 1030 Newton, E. R., Mann, A. W., Tofflemire, B. M., et al.
1031 2019, *ApJ*, 880, L17
- 1032 Oh, S., Price-Whelan, A. M., Hogg, D. W., Morton,
1033 T. D., & Spergel, D. N. 2017, *AJ*, 153, 257
- 1034 Owen, J. E. 2020, *MNRAS*, 498, 5030
- 1035 Owen, J. E., & Wu, Y. 2013, *ApJ*, 775, 105
—. 2016, *ApJ*, 817, 107
- 1037 Palle, E., Oshagh, M., Casasayas-Barris, N., et al. 2020,
1038 *A&A*, 643, 25
- 1039 Pavlidou, T., Scholz, A., & Teixeira, P. S. 2021,
1040 *MNRAS*, 503, 3232
- 1041 Pecaut, M. J., & Mamajek, E. E. 2013, *ApJS*, 208, 9
- 1042 Pecaut, M. J., & Mamajek, E. E. 2016, *MNRAS*, 461,
1043 794
- 1044 Plavchan, P., Barclay, T., Gagné, J., et al. 2020, *Nature*,
1045 582, 497
- 1046 Poppenhaeger, K., Ketzer, L., & Mallonn, M. 2021,
1047 *MNRAS*, 500, 4560
- 1048 Randich, S., Tognelli, E., Jackson, R., et al. 2018, *A&A*,
1049 612, A99
- 1050 Ratzenböck, S., Meingast, S., Alves, J., Möller, T., &
1051 Bomze, I. 2020, *A&A*, 639, A64
- 1052 Rebull, L. M., Stauffer, J. R., Bouvier, J., et al. 2016,
1053 *AJ*, 152, 113
- 1054 Reinhold, T., & Hekker, S. 2020, *A&A*, 635, A43
- 1055 Ricker, G. R., Winn, J. N., Vanderspek, R., et al. 2015,
1056 *JATIS*, 1, 014003
- 1057 Rizzuto, A. C., Mann, A. W., Vanderburg, A., Kraus,
1058 A. L., & Covey, K. R. 2017, *AJ*, 154, 224
- 1059 Rizzuto, A. C., Newton, E. R., Mann, A. W., et al. 2020,
1060 *AJ*, 160, 33
- 1061 Roccatagliata, V., Franciosini, E., Sacco, G. G.,
1062 Randich, S., & Sicilia-Aguilar, A. 2020, *A&A*, 638,
1063 A85
- 1064 Roettenbacher, R. M., Monnier, J. D., Korhonen, H.,
1065 et al. 2017, *ApJ*, 849, 120
- 1066 Röser, S., & Schilbach, E. 2020, *A&A*, 638, A9
1067 Salvatier, J., Wieckiā, T. V., & Fonnesbeck, C. 2016,
1068 PyMC3: Python probabilistic programming
1069 framework
- 1070 Scargle, J. D. 1982, *ApJ*, 263, 835
- 1071 Scott, N. J., Howell, S. B., Horch, E. P., & Everett,
1072 M. E. 2018, *PASP*, 130, 054502
- 1073 Scott, N. J., Howell, S. B., Gnilka, C. L., et al. 2021,
1074 *Frontiers in Astronomy and Space Sciences*, 8, 138
- 1075 Seifahrt, A., Stürmer, J., Bean, J. L., & Schwab, C.
1076 2018, in *SPIE Conference Series*, Vol. 10702,
1077 *Ground-based and Airborne Instrumentation for
Astronomy VII*, ed. C. J. Evans, L. Simard, &
1078 H. Takami, 107026D
- 1079 Shapiro, A. I., Solanki, S. K., Krivova, N. A., Yeo,
1080 K. L., & Schmutz, W. K. 2016, *A&A*, 589, A46
- 1081 Shporer, A., Zhou, G., Vanderburg, A., et al. 2017,
1082 *ApJL*, 847, L18
- 1083 Skrutskie, M. F., Cutri, R. M., Stiening, R., et al. 2006,
1084 *AJ*, 131, 1163
- 1085 Smith, J. C., Morris, R. L., Jenkins, J. M., et al. 2016,
1086 *PASP*, 128, 124501
- 1087 Smith, J. C., Stumpe, M. C., Jenkins, J. M., et al. 2017,
1088 *Kepler Science Document*, 8
- 1089 Soderblom, D. R., Hillenbrand, L. A., Jeffries, R. D.,
1090 Mamajek, E. E., & Naylor, T. 2014, *Protostars and
Planets VI*, 219
- 1091 Spake, J. J., Sing, D. K., Evans, T. M., et al. 2018,
1092 *Nature*, 557, 68
- 1093 Stassun, K. G., Oelkers, R. J., Paegert, M., et al. 2019,
1094 *AJ*, 158, 138
- 1095 Stauffer, J. R., Hartmann, L. W., Prosser, C. F., et al.
1096 1997, *ApJ*, 479, 776
- 1097 Stefansson, G., Mahadevan, S., Maney, M., et al. 2020,
1098 *AJ*, 160, 192
- 1099 Stephenson, C. B. 1959, *PASP*, 71, 145
- 1100 Strassmeier, K. G. 2009, *Astronomy and Astrophysics
Review*, 17, 251
- 1101 Tenenbaum, P., Christiansen, J. L., Jenkins, J. M., et al.
1102 2012, *ApJS*, 199, 24
- 1103 Theano Development Team. 2016, *arXiv e-prints*,
1104 abs/1605.02688
- 1105 Thompson, S. E., Coughlin, J. L., Hoffman, K., et al.
1106 2018, *ApJS*, 235, 38
- 1107 Tian, H.-J. 2020, *ApJ*, 904, 196
- 1108 Tofflemire, B. M., Rizzuto, A. C., Newton, E. R., et al.
1109 2021, *AJ*, 161, 171
- 1110 Ujjwal, K., Kartha, S. S., Mathew, B., Manoj, P., &
1111 Narang, M. 2020, *AJ*, 159, 166
- 1112 Van Eylen, V., Agentoft, C., Lundkvist, M. S., et al.
1113 2018, *MNRAS*, 479, 4786

- 1117 Van Eylen, V., Albrecht, S., Huang, X., et al. 2019, *AJ*,
1118 **157, 61**
- 1119 Villa Vélez, J. A., Brown, A. G. A., & Kenworthy,
1120 M. A. 2018, *RNAAS*, **2**, 58
- 1121 Vissapragada, S., Knutson, H. A., Jovanovic, N., et al.
1122 2020, *AJ*, **159**, 278
- 1123 Vogt, S. S., Allen, S. L., Bigelow, B. C., et al. 1994,
1124 SPIE Conference Series, ed. D. L. Crawford & E. R.
1125 Craine, Vol. 2198
- 1126 Wang, L., & Dai, F. 2019, *ApJL*, **873**, L1
- 1127 Wenger, M., Ochsenbein, F., Egret, D., et al. 2000,
1128 *A&AS*, **143**, 9
- 1129 Wirth, C. P., Zhou, G., Quinn, S. N., et al. 2021, *ApJL*,
1130 **917**, L34
- 1131 Wu, Y. 2019, *ApJ*, **874**, 91
- 1132 Yee, S. W., Petigura, E. A., & von Braun, K. 2017, *ApJ*,
1133 **836**, 77
- 1134 Yelda, S., Lu, J. R., Ghez, A. M., et al. 2010, *ApJ*, **725**,
1135 331
- 1136 Zari, E., Hashemi, H., Brown, A. G. A., Jardine, K., &
1137 de Zeeuw, P. T. 2018, *A&A*, **620**, A172
- 1138 Zhou, G., Winn, J. N., Newton, E. R., et al. 2020, *ApJ*,
1139 **892**, L21
- 1140 Zhou, G., Quinn, S. N., Irwin, J., et al. 2021, *AJ*, **161**, 2

1141

APPENDIX

1142

A. YOUNG, AGE-DATED, AND AGE-DATEABLE STAR COMPILATION

1143 The v0.6 CDIPS target catalog (Table 3) includes stars that are young, age-dated, and age-dateable. By
 1144 “age-dateable”, we mean that the stellar age should be measurable at greater precision than that of a typical
 1145 FGK field star, through either isochronal, gyrochronal, or spectroscopic techniques. As in Bouma et al.
 1146 (2019), we collected stars that met these criteria from across the literature. Table 4 gives a list of the studies
 1147 included, and brief summary statistics. The age measurement methodologies adopted by each study differ: in
 1148 many, spatial and kinematic clustering has been performed on the Gaia data, and ensemble isochrone fitting
 1149 of the resulting clusters has been performed (typically focusing on the turn-off). In other studies however,
 1150 the claim of youth is based on the location of a single star in the color-absolute magnitude diagram, or on
 1151 spectroscopic information.

1152 One major change in Table 3 relative to the earlier iteration from Bouma et al. (2019) is that the extent
 1153 of Gaia-based analyses has now matured to the point that we can neglect pre-Gaia cluster memberships,
 1154 except for a few cases with spectroscopically confirmed samples of age-dated stars. The membership lists for
 1155 instance of Kharchenko et al. (2013) and Dias et al. (2014) (MWSC and DAML) are no longer required. This
 1156 is helpful for various post-processing projects, since the field star contamination rates were typically much
 1157 higher in these catalogs than in the newer Gaia-based catalogs.

1158 The most crucial parameters of a given star for our purposes are the Gaia DR2 `source_id`, the cluster
 1159 or group name (`cluster`), and the `age`. Given the hierarchical nature of many stellar associations, we
 1160 do not attempt to resolve the cluster names to a single unique string. The Orion complex for instance can
 1161 be divided into almost one hundred kinematic subgroups (Kounkel et al. 2018). Similar complexity applies
 1162 to the problem of determining homogeneous ages, which we do not attempt to resolve. Instead, we simply
 1163 merged the cluster names and ages reported by various authors into a comma-separated string.

1164 This means that the `age` column can be null, for cases in which the original authors did not report an age,
 1165 or for which a reference literature age was not readily available. Nonetheless, since we do prefer stars with
 1166 known ages, we made a few additional efforts to populate this column. When available, the age provenance
 1167 is from the original analysis of the cluster. In a few cases however we adopted other ages when string-
 1168 based cross-matching on the cluster name was straightforward. In particular, we used the ages determined
 1169 by Cantat-Gaudin et al. (2020) to assign ages to the clusters from Gaia Collaboration et al. (2018a), Cantat-
 1170 Gaudin et al. (2018), Castro-Ginard et al. (2020), and Cantat-Gaudin & Anders (2020).

1171 The catalogs we included for which ages were not immediately available were those of Cotten & Song
 1172 (2016), Oh et al. (2017), Zari et al. (2018), Gagné et al. (2018a), Gagné et al. (2018b), Gagné & Faherty
 1173 (2018), and Ujjwal et al. (2020). While in principle the moving group members discussed by Gagné et al.
 1174 (2018a,b); Gagné & Faherty (2018) and Ujjwal et al. (2020) have easily associated ages, our SIMBAD cross-
 1175 match did not retain the moving group identifiers given by those studies, which should therefore be recovered
 1176 using tools such as BANYAN Σ (Gagné et al. 2018b). We also included the SIMBAD object identifiers `TT*`,
 1177 `Y*O,Y*?, TT?`, and `pMS*`. Finally, we included every star in the NASA Exoplanet Archive planetary system
 1178 (`ps`) table that had a Gaia identifier available (Akeson et al. 2013). If the age had finite uncertainties, we also
 1179 included it, since stellar ages determined through the combination of isochrone-fitting and transit-derived
 1180 stellar densities typically have higher precision than from isochrones alone.

1181 For any of the catalogs for which Gaia DR2 identifiers were not available, we either followed the spatial
 1182 (plus proper-motion) cross-matching procedures described in Bouma et al. (2019), or else we pulled the
 1183 Gaia DR2 source identifiers associated with the catalog from SIMBAD. We consequently opted to drop the
 1184 `ext_catalog_name` and `dist` columns maintained in Bouma et al. (2019), as these were only popu-
 1185 lated for a small number of stars. The technical manipulations for the merging, cleaning, and joining were
 1186 performed using pandas (McKinney 2010). The eventual cross-match (using the Gaia DR2 `source_id`)
 1187 against the Gaia DR2 archive was performed asynchronously on the Gaia archive website.

1188

B. THE TRANSIT ASYMMETRY

1189

B.1. *How Robust is the Asymmetric Transit?*

1190 As a means of exploring the robustness of the transit asymmetry, Figures 9, 10, and 11 show the Kepler data
 1191 binned in three ways: over Kepler quarters, Julian years, and quartiles of local slope. Over Kepler quarters
 1192 (Figure 9), Quarter 6 shows the strongest asymmetry: a deviation of about 3 ppt from expectation. Quarter

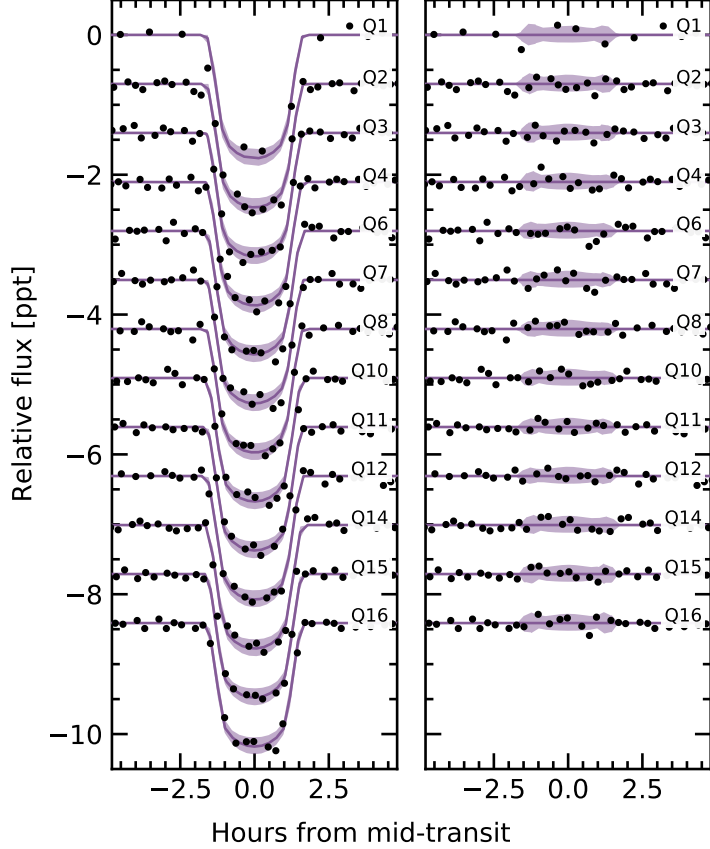


Figure 9. Transit model residuals through time (binned by Kepler quarter). *Left:* Phase-folded transit of Kepler 1627b, with stellar variability removed. Black points are binned to 20 minute intervals. The 2σ model uncertainties and the maximum *a posteriori* model are shown as the faint purple band, and the dark purple line. *Right:* As on the left, with the transit removed.

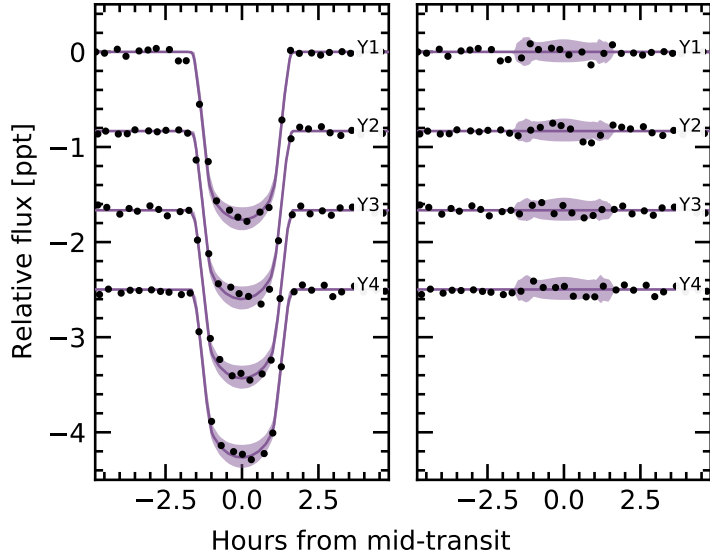


Figure 10. Transit model residuals through time (binned by year of observation). *Left:* Phase-folded transit of Kepler 1627b, with stellar variability removed. Points and models are as in Figure 9. *Right:* As on the left, with the transit removed.

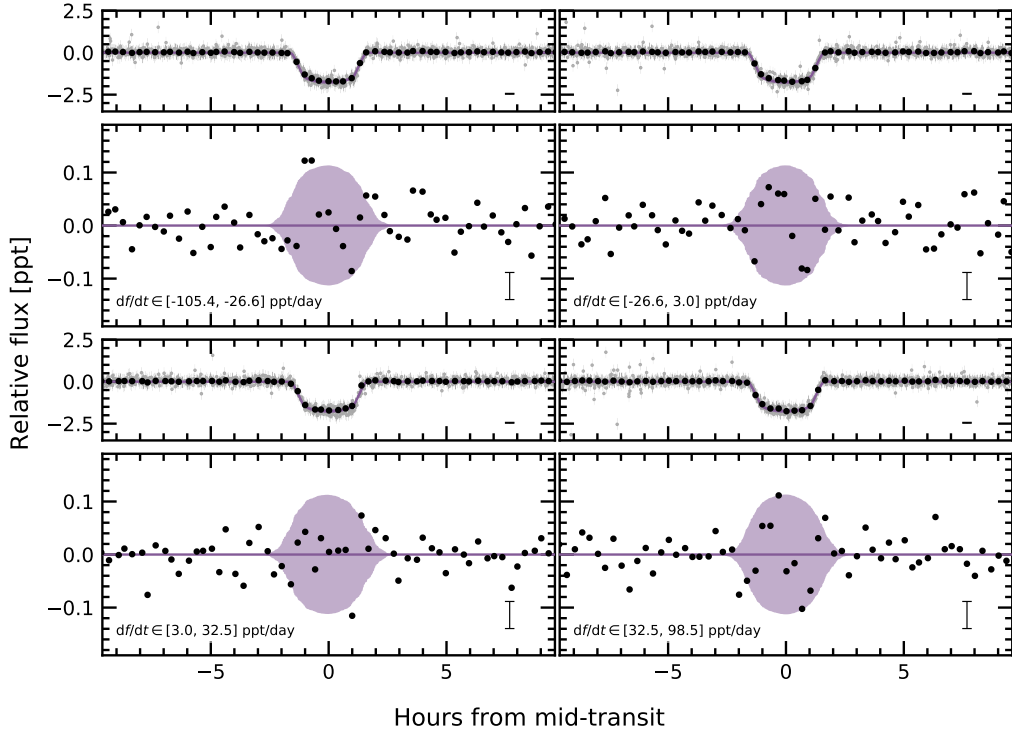


Figure 11. Transit models and residuals, binned by quartiles in the local slope of the light curve. Representative uncertainties for the black points (binned at 20 minute intervals) are shown in the lower right of each panel. A similar transit asymmetry to that shown in Figure 5 seems to be present in three of the four bins.

1193 7 shows an anomaly at roughly the same transit phase. Year 2 correspondingly shows the strongest anomaly
 1194 out of any year in Figure 10; the asymmetry is visually apparent however in each of the four years.

1195 To bin by quartiles in local slope, we used our measurements of the local linear slopes in each of the
 1196 observed transit windows (144 transits total). Four outlier transits were removed, leaving 140 transits. These
 1197 were then divided into quartiles, so that each panel shows 35 transits binned together. The exact light curve
 1198 slope intervals are listed in the lower left panels of Figure 11. Binned by local slope quartiles (Figure 11),
 1199 the asymmetry is visually present in three of the four quartiles: the only bin in which it does not appear is
 1200 $df/dt \in [3.0, 32.5] \text{ ppt day}^{-1}$.

1201 Within the theory presented by Mazeh et al. (2015), unresolved starspot crossings cause the weak correlation
 1202 between TTVs and the local light curve slope (Figure 6). In this model, we would expect the light curves
 1203 with the most negative local slopes to have the largest positive TTVs, due to spot crossing events during the
 1204 latter half of transit. The upper-left panel of Figure 11 agrees with this expectation. However, we would also
 1205 expect the sign of the effect to reverse when considering the most positive local slopes (most negative TTVs).
 1206 The lower-right panel of Figure 11 contradicts this expectation: the residual in both cases maintains the same
 1207 parity! On the one hand, this shows that the residual is not dependent on the local light curve slope, which
 1208 lowers the likelihood that it might be an artifact of our detrending methods. On the other, it raises the question
 1209 of whether unresolved starspot crossings are indeed the root cause of the correlation shown in Figure 6. While
 1210 we do not have a solution to this contradiction, the injection-recovery tests discussed in Section 4.1.3 provide
 1211 some assurance that the TTV-slope correlation is not simply a systematic artifact.

1212 B.2. Interpretation

1213 The transit asymmetry seems robust against most methods of binning the data, though with some caveats
 1214 (e.g., the “middle quartile” in local flux, $df/dt \in [3.0, 32.5] \text{ ppt day}^{-1}$, where the asymmetry does not appear).
 1215 Nonetheless, if the asymmetric were systematic we might expect its parity to reverse as a function of the sign
 1216 of the local slope, and it does not. We therefore entertained four possible astrophysical explanations: gravity
 1217 darkening, transit timing variations, spot-crossing events, and a persistent asymmetric dusty outflow.

1218 Gravity darkening is based on the premise that the rapidly rotating star is oblate, and brighter near the
 1219 poles than the equator (e.g., Masuda 2015). The fractional transit shape change due to gravity darkening
 1220 is on the order of $(P_{\text{break}}/P_{\text{rot}})^2$, for P_{break} the break-up rotation period, and P_{rot} the rotation period. Using

the parameters from Table 2, this yields an expected 0.14% distortion of the ≈ 1.8 ppt transit depth: *i.e.*, an absolute deviation of ≈ 2.5 ppm. The observed residual has a semi-amplitude of ≈ 50 ppm. Since the expected signal is smaller than the observed anomaly by over an order of magnitude, gravity darkening seems to be an unlikely explanation.

The scenario of transit timing variations (TTVs) producing the asymmetry seems unlikely because the transit timing variations we do observe are correlated with the local light curve slope, which increases roughly as much as it decreases. From our analysis, the mean TTV and its standard deviation are 0.66 ± 5.53 min; similarly the mean local slope and its standard deviation are 0.59 ± 45.50 ppt day $^{-1}$. There is therefore little expectation for TTVs to produce the asymmetry. A separate line of argument comes from Figure 11. If the local slope were essential to producing the transit asymmetry, we would expect that in the largest df/dt bin, $df/dt \in [3.0, 32.5]$ ppt day $^{-1}$, the sign of the asymmetry would reverse. We do not see evidence for this being the case.

The third and related possibility is that of starspot crossings. Young stars have higher spot-covering fractions than old stars (*e.g.*, Morris 2020). Young solar-type stars may also host dark starspots at high stellar latitudes (*e.g.*, EK Dra; Strassmeier 2009), though interferometric imaging of spotted giant stars has shown different starspot latitude distributions than those inferred from Doppler imaging (Roettenbacher et al. 2017). Regardless, for any spot-crossing anomalies to add coherently over the 140 Kepler transits, it seems likely that we would need either for spots to be persistent at a particular latitude (and for the planetary orbit to be somewhat misaligned), or for a “stroboscopic” longitudinal phasing (*e.g.*, Dai et al. 2018). For our system, $P_{\text{orb}}/P_{\text{rot}} \approx 2.76$, which means that every 4 transits and 11 stellar rotations, the planet crosses over roughly the same stellar longitude, which might enable the necessary phasing if the spot-groups are large and long-lived. Unfortunately, the S/N per Kepler transit is ≈ 8 , which renders individual spot-crossing events unresolved. This explanation seems marginally plausible, mainly because the expected spot-crossing anomaly amplitudes (≈ 100 ppm) resemble the observed amplitude of the asymmetry (≈ 50 ppm). One issue with this explanation however is that there is no reason to expect starspot crossing events to last exactly half the transit duration.

A persistent feature of the planet itself might therefore be needed to explain the transit asymmetry. An asymmetric outflow from the planet’s atmosphere could at least geometrically meet the requirements (*e.g.*, McCann et al. 2019). To explain the asymmetric transit, a small, dense component would lead the planet, and a long, more rarefied (and variable) component would trail it. This might also explain the slight flux decrement visible for ~ 1 hour pre-ingress (Figure 5). The amplitude of the asymmetry is roughly in line with theoretical expectations for dusty outflows (Wang & Dai 2019), and based on the planet’s size, its mass is likely in a regime where such outflows are possible. Out of the four explanations discussed, this one at least theoretically seems the most plausible. By composition, the expectation would be that the envelope is mostly hydrogen and helium gas, with a dust or haze component providing the broadband opacity in the Kepler bandpass. A natural path for testing this idea would be to observe additional transits of the planet in hydrogen absorption, metastable helium absorption, or across a broad wavelength range in the near-infrared.

C. SPECTROSCOPY AND PHOTOMETRY DURING THE TRANSIT OF 2021 AUG 7

We monitored Kepler 1627 with Keck/HIRES before, during, and after transit on the night of 2021 Aug 7. We used the iodine cell for wavelength calibration, and extracted the 1-D spectra using the standard California Planet Survey pipeline (Howard et al. 2010). The airmass ranged between 1.1 and 2.2 from the start through the end of observations; the seeing ranged from $1.^{\prime\prime}1$ at the beginning to $1.^{\prime\prime}5$ at the end. We also simultaneously observed across *griz* bands using MuSCAT3 at Haleakalā Observatory on Maui, HI. Performing aperture photometry on the latter image stack yielded the data given in Table 5.

We considered two approaches to measuring the velocities: in the first, hereafter “Method 1”, we cross-correlated against a template found via spectral classification with SpecMatch-Emp (Yee et al. 2017). In “Method 2”, we used a high S/N template of V1298 Tau. Although V1298 Tau is cooler than Kepler 1627A by ≈ 500 K, it has a comparable amount of line-broadening ($v \sin i = 23$ km s $^{-1}$), and a comparable level of stellar activity. The mean and standard deviation of the internal RV uncertainties averaged over all epochs were 16.2 ± 1.1 m s $^{-1}$ from Method 1, and 12.6 ± 0.6 m s $^{-1}$ from Method 2. The corresponding time-averaged reduced χ^2 from the template match was 1.57 ± 0.04 (Method 1) and 1.30 ± 0.02 (Method 2). Given these diagnostics, we adopted the velocities from the second approach, which are reported in Table 6.

Figure 7 shows the results. The MuSCAT3 photometry shows the expected starspot trend, along with the transit and what is likely a chromatic starspot crossing event at JD – 2459433 = 0.955. The radial velocities decrease by ≈ 250 m s $^{-1}$ over the six hour window. This decrease in RV is correlated with a decrease in the S-indices derived from the Ca HK lines. One outlying RV point is apparent shortly before egress; it is temporally coincident with an outlying value in the S-index time series.

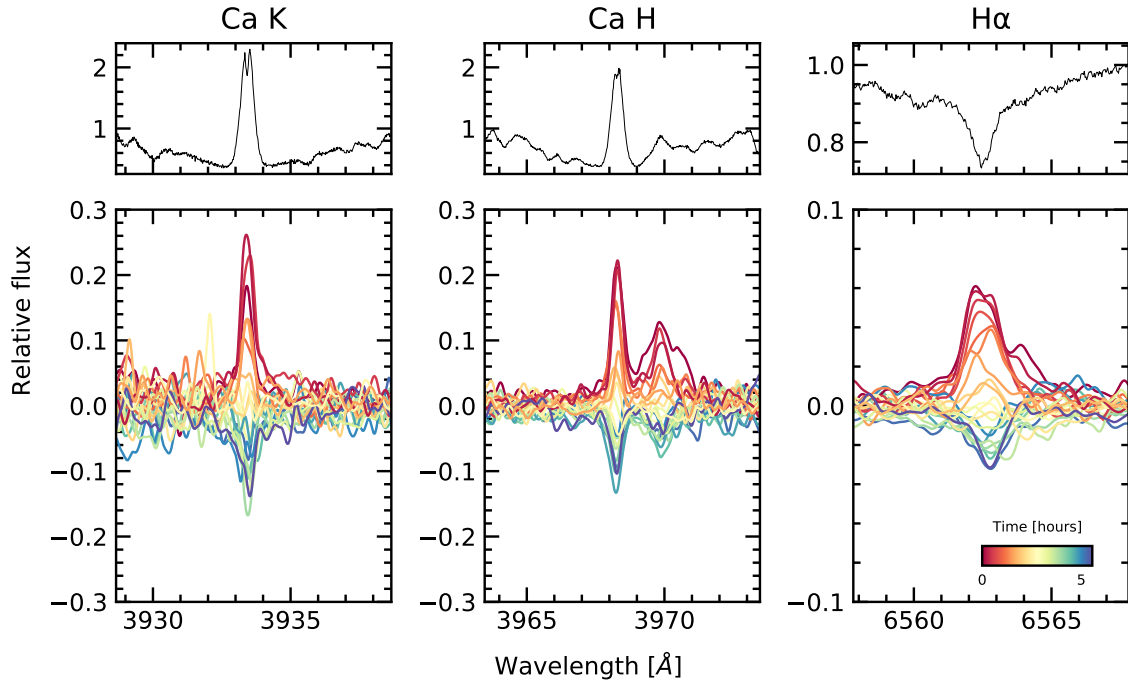


Figure 12. Spectroscopic activity indicators during the transit of 2021 Aug 7. The *top panels* show the median line profiles Ca K, Ca H, and H α line profiles from the HIRES spectra. The *lower panels* show the differences of each individual spectrum relative to the median spectrum. The bump in the red wing of Ca H is He. The spectra in the lower panels are smoothed for visualization purposes.

Overall, we expect the dominant trends in both the photometry and radial velocities to be caused by starspots on the stellar photosphere rotating into and out of view. The plasma in the leading and receding limbs of the stellar disk has an apparent line-of-sight velocity of $\pm 20 \text{ km s}^{-1}$. Over 10% of a rotation cycle ($P_{\text{rot}} = 2.6 \text{ days}$), spots near these limbs come into and out of view, modulate the stellar velocity profile, and can thereby produce the overall $\approx 250 \text{ m s}^{-1}$ trend. The Ca HK and H α emission profiles support this interpretation; Figure 12 shows that each line gradually decreases in intensity over the course of the six hour sequence.

The expectation however is for the starspot-induced signals to be smooth, at worst with contributions at $0.5 P_{\text{rot}}$ or $0.25 P_{\text{rot}}$ (Klein & Donati 2020). We therefore fitted the RVs using the Hirano et al. (2010, 2011) models for the Rossiter-McLaughlin (RM) effect, and allowed for an optional linear and quadratic trend in time to fit the $\approx 250 \text{ m s}^{-1}$ spot-induced trend. We followed the methodology developed by Stefansson et al. (2020). We allowed the sky-projected obliquity, the projected stellar equatorial velocity, and the Gaussian dispersion of the spectral lines to vary, and fixed the limb-darkening using the V-band tabulation from Claret & Bloemen (2011). We assumed a Gaussian prior on $v \sin i$ and a/R_{\star} from Table 1, and also allowed for a white-noise jitter term to be added in quadrature to the measurement uncertainties. We used a 15 minute exposure time to numerically evaluate the model.

The quadratic model with the RM effect is shown in Figure 7; the jitter term is incorporated in the model uncertainties, but not the plotted measurement uncertainties. The plotted measurement uncertainties are the internal uncertainties on the RVs ($\approx 13 \text{ m s}^{-1}$), and are dominated by the $v \sin i$ broadening. However, between exposures, the RVs show significant additional scatter that is not captured by the slow quadratic trend. The white-noise jitter for this particular model is $\sigma_{\text{RV}} = 27^{+6}_{-5} \text{ m s}^{-1}$, which is comparable to the expected RM anomaly of $\Delta v_{\text{RM}} \approx f_{\text{LD}} \cdot \delta \cdot v \sin i \cdot \sqrt{1 - b^2} \approx 20 \text{ m s}^{-1}$, assuming a perfectly aligned orbit.

The presence of this additional scatter prevents a convincing detection of the RM effect. The reason can be understood via model comparison. If we compare the model with a quadratic trend and the RM effect against a model with a linear trend and the RM effect, or even a model with no RM effect at all, then the respective

Bayesian Information Criterion (BIC) values are as follows.

$$\begin{aligned} \text{BIC} &= 227.1 \quad (\text{Quadratic+RM}) \\ \text{BIC} &= 231.1 \quad (\text{Linear+RM}) \\ \text{BIC} &= 221.4 \quad (\text{Only Quadratic}). \end{aligned} \quad (\text{C1})$$

1298 There is therefore no evidence to prefer the model with the RM effect against a model that only accounts
 1299 for the stellar variability. The “only quadratic” model does particularly well because it can inflate the jitter
 1300 term to account for scatter during the transit (even if the scatter contains astrophysics!), and it has fewer free
 1301 parameters. However, we cannot justify a physical prior on the jitter term, because we do not understand
 1302 the origin of the exposure-to-exposure scatter. As noted above, the velocity deviations from starspots are
 1303 expected to have contributions at the stellar rotation frequency, or harmonics thereof. This jitter is present on
 1304 the exposure timescale (15 minutes), which is only 0.4% of the stellar rotation period; it is not obvious that
 1305 starspots would be the culprit.

1306 The amplitude of both the spot-induced trend and the jitter are somewhat larger than recent comparable
 1307 measurements in systems such as AU Mic (Palle et al. 2020), DS Tuc (Montet et al. 2020; Zhou et al. 2020)
 1308 and TOI 942 (Wirth et al. 2021). One possible explanation for the jitter is that it is astrophysical in origin,
 1309 and that it is caused by some novel process operating on the surface of Kepler 1627A. Another possibility
 1310 is that our RV analysis underestimates our measurement uncertainties; in order to achieve the requisite time-
 1311 sampling the S/N per resolution element in our spectra was 70 to 80, which is lower than desired for deriving
 1312 high-precision velocities. In addition, the rapid rotation of the star could affect accuracy of the uncertainties
 1313 from the velocity extraction. Observations at higher S/N are necessary to distinguish these two possibilities,
 1314 and remain worthwhile in order to clarify the orbital geometry of Kepler 1627Ab. Useful next steps would
 1315 include transit observations with a stabilized spectrograph in the optical (e.g., Gibson et al. 2016; Seifahrt
 1316 et al. 2018), or in the near-infrared (e.g., Feinstein et al. 2021).

Table 5. MuSCAT3 photometry of Kepler 1627.

Time [BJD _{TDB}]	Rel. Flux	Rel. Flux Err.	Bandpass
2459433.829202	0.99719	0.00091	g
2459433.829324	0.99849	0.00112	r
2459433.829117	0.99611	0.00116	i
2459433.829406	0.99941	0.00136	z

NOTE— Table 5 is published in its entirety in a machine-readable format. Example entries are shown for guidance regarding form and content.

Table 6. Kepler 1627 radial velocities.

Time [BJD _{TDB}]	RV [m s^{-1}]	σ_{RV} [m s^{-1}]	S-value
2459433.801306	152.97	12.29	0.7355
2459433.812255	100.5	13.23	0.7434

NOTE— Table 6 is published in its entirety in a machine-readable format. Example entries are shown for guidance regarding form and content.

D. FLARE ANALYSIS

1318 In addition to the 3.9 years of long cadence data,
 1319 short cadence (1-minute) Kepler observations were
 1320 acquired over 97.7 days during Quarter 15. The
 1321 short cadence light curve shows a higher rate of
 1322 flaring than visible in the long cadence data (Figure
 1323 13). We analyzed the short cadence light curve
 1324 and its flares according to the following procedure.

- 1325 1. Fit the starspot-induced variability using a
 1326 Gaussian Process with a SHOTerm kernel,
 1327 a white-noise jitter term, and the mean flux.
- 1328 2. Select points more than twice the median ab-
 1329 solute deviation from the residual, and ex-
 1330 clude them from the light curve (these points
 1331 include the flares). Repeat Step 1.

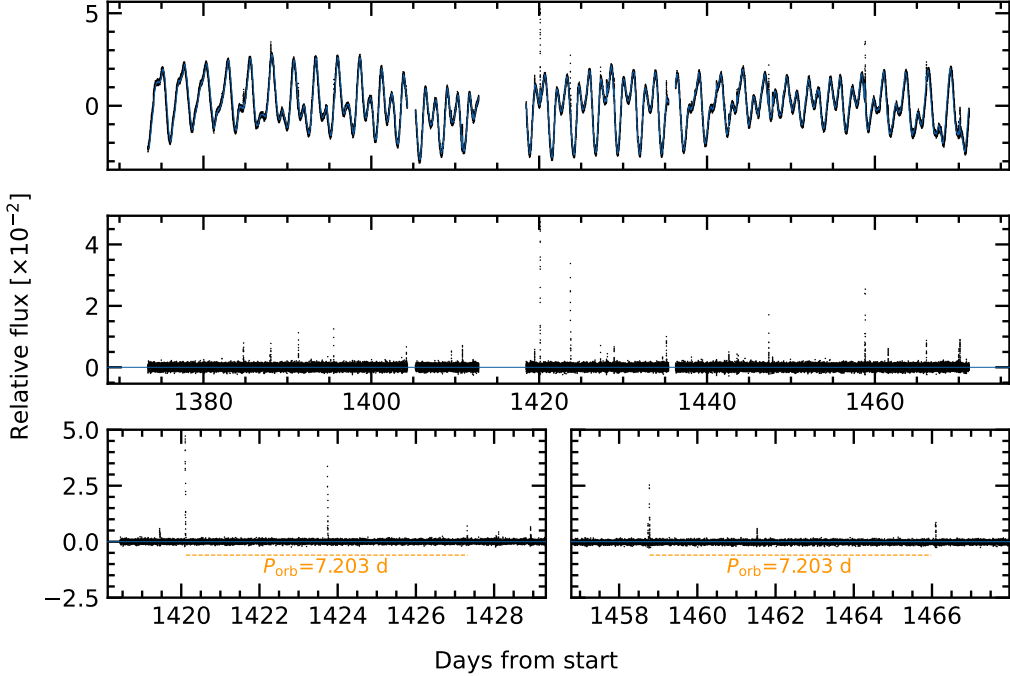


Figure 13. Flares in Kepler 1627. *Top:* The 1-minute cadence Kepler data (black points) is shown with a stellar variability model superposed (blue line). *Middle:* Residual after subtracting the stellar variability model. Flares appear as spikes. *Bottom:* Zooms of the brightest, and third-brightest flares. A timing coincidence – that both flares have “successors” approximately one orbital period after the initial event – is emphasized.

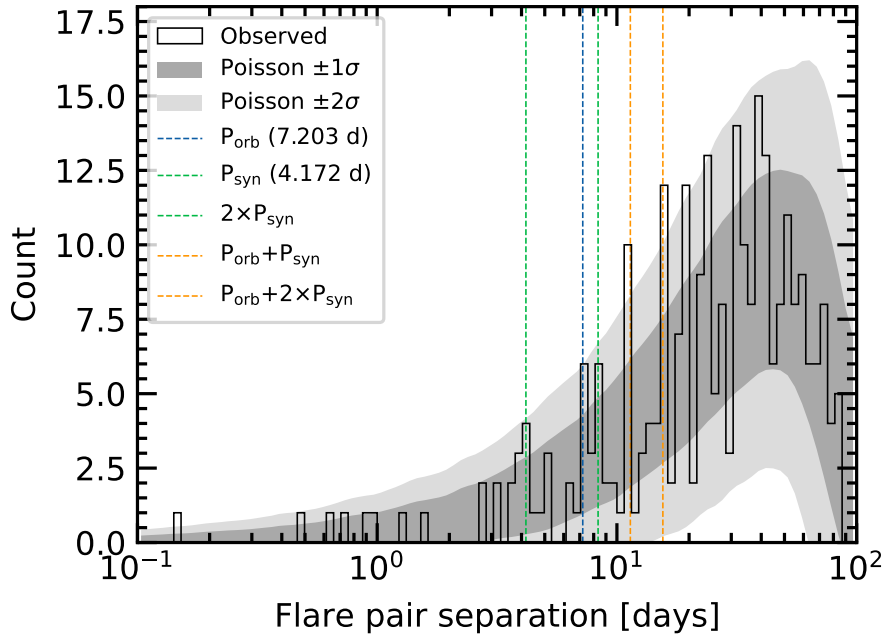


Figure 14. Statistics of inter-flare arrival times. 24 flares were recorded with amplitudes exceeding 0.5% over the 97.7 days of short cadence observations. The histogram of the time intervals between every possible pair of flares is shown in black. Some plausibly important timescales for star-planet interactions, namely the planetary orbital period and synodic period (the orbital period as seen from the rotating stellar frame) are shown along with their linear combinations. Monte Carlo draws from a Poisson distribution are shown with the gray bands. While peaks in the observed distribution do coincide with some of the “special periods”, the statistical evidence for a non-Poissonian process driving the flares does not clear the 5σ threshold.

1332 3. Using the residual from Step 2, identify all
1333 flares, requiring them to be at least 20 ca-
1334 dences apart, at least 7 median absolute de-
1335 viations above the median baseline, and last-
1336 ing at least 2 cadences in duration. Build the
1337 mask spanning these times, from 5 minutes
1338 before each flare begins to 2.5 minutes after
1339 the final flare cadence. Repeat Step 1 a final
1340 time.

1341 The final step of flare identification and fitting was
1342 performed using `altaipony` (Davenport 2016;
1343 Ilin et al. 2021). The analytic flare model is from
1344 Davenport et al. (2014) and it parametrizes the flare
1345 with a start time, an exponential lag time, and an
1346 amplitude.

1347 There were $N_f = 24$ flares that exceeded 0.5% in
1348 relative flux during the short cadence observations.
1349 These 24 flares spanned a total of 6.5 hours (~ 15
1350 minutes per flare). Inspecting the data, we noticed
1351 a coincidence in the flare arrival times. The co-
1352 incidence is that despite the low flare duty cycle,
1353 one orbital period after the brightest flare, a second
1354 flare followed. This and a similar event are shown
1355 in Figure 13. The timing error is good to a $\approx 0.2\%$
1356 difference from the orbital period, which given the
1357 duty cycle seems *a priori* unlikely. If we consider
1358 flares falling within 2% of the planet’s orbital pe-
1359 riod after a previous flare, then 4 of the 24 flare
1360 events have candidate “successors”.

1361 As with any coincidence, if one does not have a
1362 firm prediction, it is difficult to assess whether a
1363 surprise is statistically significant. Since our sur-
1364 prise was specifically at the inter-arrival time of
1365 certain flares coinciding with special time inter-
1366 vals, we performed the following analysis. First,
1367 we considered all unordered pairs of flares. For
1368 N flares there are $\binom{N}{2}$ such pairs (for our case,
1369 276 pairs). We then compared the distribution of
1370 the pair separations against that of a Poisson dis-
1371 tribution. Specifically, we drew $N_f = 24$ samples
1372 from a Poisson distribution with $\lambda = \Delta t / N_f$, for
1373 $\Delta t = 97.7$ days the total duration of the observa-
1374 tions, and repeated the draw 10^3 times with unique
1375 random seeds.

1376 Figure 14 shows the results. The vertical lines
1377 in the figure show the planetary orbital period,
1378 the synodic period $P_{\text{syn}} = (P_{\text{rot}}^{-1} - P_{\text{orb}}^{-1})^{-1}$, and lin-
1379 ear combinations thereof. The tidal period (half
1380 the synodic period) is not shown. The bins are
1381 logarithmically spaced to give 100 bins between
1382 the minimum and maximum ordinate values. The
1383 gray bands express the range of values observed
1384 from the Poissonian draws. While it does seem
1385 like an odd coincidence for peaks in the observed
1386 flare arrival time distribution to coincide with the
1387 locations of these “special intervals”, the statisti-
1388 cal evidence for a non-Poissonian process driving

1389 the flares does not seem especially overwhelming.
1390 More quantitatively, the peaks observed at the or-
1391 bital and synodic periods are within the $\pm 2\sigma$ range
1392 of a Poissonian process, and those at $P_{\text{orb}} + P_{\text{syn}}$ and
1393 $P_{\text{orb}} + 2P_{\text{syn}}$ are only slightly above this range. With
1394 that said, future analyses of these data by investiga-
1395 tors with more knowledge of this topic could very
1396 well yield more quantitative insights. Such analy-
1397 ses should keep in mind an important caveat: the
1398 amplitude distribution of M-dwarf flares extends
1399 up to many times the quiescent flux (see Figure 7 of
1400 Günther et al. 2020). A flare on Kepler 1627B pro-
1401 ducing double its quiescent white-light flux would
1402 yield a $\approx 1\%$ apparent amplitude. Such flares could
1403 represent a significant fraction of those in the Ke-
1404 pler observations.